Fracture of Ti₃C₂-TiO₂ Atomically Thin Films

Jianyu Dai¹, Congjie Wei¹, Chenglin Wu^{1*}

¹ Zachry Department of Civil and Environmental Engineering, Texas A&M University, College Station, TX, USA

Abstract

MXene exhibits outstanding electrical conductivity, but its susceptibility to oxidation can impede its conductivity potential. While there is extensive research on the electrical, mechanical properties, and fracture behavior of pure MXene, the exploration of the oxidized MXene is rare, especially for the commonly observed Ti₃C₂-TiO₂ mixtures. In this study, we conducted molecular dynamics (MD) and Density Functional Theory (DFT) approaches and, for the first time, discovered three stable crystal structures of pure MXene with attached TiO₂ layers: Loose, Comb, and Tight. For each of these structures, we investigated the anisotropic mechanical and fracture behaviors based on two loading scenarios: ribbon and pre-cracked single layers. The results indicate that the anisotropic behavior is predominantly manifested in Loose and Tight structures. The structural asymmetry of Comb results in a larger and evolving cohesive zone. The direction of the TiO₂ layer-MXene interface bonds influences the material's strength, with the Tight structure exhibiting the highest resistance to fracture.

1. Introduction

Titanium carbides ($Ti_3C_2T_x$) are the most prevalent type of MXene, which belong to the family of 2D materials known for their exceptional combination of functional properties. MXene, characterized by the general formula $M_{n+1}X_nT_x$, where n=1,2,3, and x represents the number of terminal groups, consisting of M (early transitional metal), X (carbon or nitrogen), and T (terminal groups). $Ti_3C_2T_x$, a representative MXene, exhibits high electrical conductivity, outstanding electromagnetic shielding capabilities, and remarkable in-plane stiffness [1-5]. These properties make it a compelling choice for various applications such as batteries, supercapacitors, and strain sensors [6-8].

Several studies have been conducted on the mechanical and fracture properties to broaden the application of MXene and its derivatives from modeling perspectives. Like other members of newly discovered 2D materials, MXene also exhibits high strength and Young's modulus [9, 10], material orientation effects [11], prone to the influence of defects [12-14]. Additionally, thanks to its stackable atomic layers to construct the MXene materials, it also has a certain degree of nonlinearity and higher toughness, compared with other 2D materials, after reaching the peak stress [11]. Wei et al. conducted molecular dynamics modeling and investigated the mechanical properties and fracture properties of pristine Ti₃C₂ and Ti₂C in the armchair and zigzag stretching directions and reported the unique anisotropic and thickness dependences [11].

Moreover, the tunable functional groups on the surfaces grant MXene more possibilities in adjusting the mechanical and electrochemical properties and broaden its application as sensing materials and more. Yorulmaz, U. et al. assessed the dynamical and mechanical stability of pristine and fully terminated MXene structures to identify potential candidates for the experiments from a density functional theory-based modeling perspective [15]. The results showed that the stability of

MXene is significantly associated with its surface structures, particularly through the presence of various terminating groups and surface chemical species. Fu et al. and Zha et al. utilized a DFT-based approach to investigate the impact of different functional groups on Ti₃C₂ MXene [16, 17]. Among the considered functional groups (F, Cl, OH, H, and O), Ti₃C₂ with -O functional groups exhibits the highest adsorption energy, in-plane planar elastic modulus, and strength enhancement. Their research provided insights into the role of functionalization in stabilizing and strengthening two-dimensional titanium carbide and emphasized the significance of surface effects on the structural and mechanical properties of carbide MXene.

On a broader scale, investigations into MXene phases have shown that fully terminated carbide-based MXene, chemically terminated with F or O groups, exhibits dynamic and mechanical stability [15, 18] which has not been observed in nitride-based MXene [19, 20]. The variations in electronic and mechanical properties of MXene phases are attributed to factors such as the type of early transition metal, the type of X atom (C and/or N), and the surface functional group employed.

However, one disadvantage that is preventing a wider application of MXene comes from the weak stability within various environmental conditions, which is closely associated with its surface structures, particularly through the presence of various surface terminating groups and chemical species. Regarding the electrical conductivity of MXene, observations in aqueous dispersions reveal a sharp decrease in electrical conductivity and mechanical properties in the presence of significant oxidation [16]. Specifically, Ti₃C₂T_x dispersed in organic solvents (acetone and acetonitrile) exhibited a rapid drop in conductivity after 14 days of aging in each medium. Interestingly, in air and solid media (frozen samples and polymer composites), the decline in conductivity occurred at a slower rate than in liquid media.

From experimental observations, TiO₂ is one of the most found structures on the surface of MXene during oxidation. Ghassemi et al. demonstrated the controlled oxidation of Ti₃C₂T_x MXene under varying conditions, showcasing that slow heating rates lead to rutile TiO₂ particle formation, while quick heating rates result in anatase TiO₂ particle formation [21, 22]. Maleski et al. dispersed Ti₃C₂T_x in various organic solvents and observed changes in color, emphasizing the distinct properties of MXene and TiO₂ particles [23-25]. This by-product of oxidation processes leads to the stretching and formation of multi-layer MXene sheets and holds promises for enhancing photocatalytic activity and other properties [23, 26], as well as the potential for improved adsorption and visible light photocatalysis combining TiO₂ with carbon facilitates electron transport, reducing recombination effects, and increases the accessible surface area of TiO₂ [27-33]. Chae's study illustrated control over the lattice structures and domain sizes of MXene-derived TiO₂ crystallites through oxidation conditions, pH, and temperature variations [34]. Moreover, the preparation of MXene/TiO₂/MoS₂ nanosheets and their nanocomposite films show the versatility of MXene-based materials for various applications, such as dielectric enhancement [35-38].

Several studies have also been conducted to explore the MXene/TiO₂ composites from modeling perspectives. Xu et al [39]. studied the interfacial structure, energetics, and electronic properties of the MXenes and anatase TiO₂ using DFT approaches and found that the functional groups on the surface of MXenes have strong influences on the interactions between these two materials. This has also been found by Ganeshan et al. [40], who explore the heterostructure of 2D lepidocrocite-type TiO₂ and Ti₃C₂ MXene using ReaxFF molecular dynamics simulations and elastic/quasi-elastic neutron scattering techniques. However, TiO₂ structures in most of these works were anatase and didn't form crystal structures with MXene. Moreover, these works mainly

focused on the electrical and photocatalytic fields while the mechanical and fracture properties left undiscussed [41, 42]. A stable crystal Ti₃C₂-TiO₂ thin film structure is still lacking in both atomic structure formation and its associated mechanical behaviors. The lattice parameters of rutile TiO₂ are entirely different from Ti₃C₂, and it is unknown what kind of structure will form when combined with Ti₃C₂. Furthermore, the introduction of TiO₂ layers would lead to the increase of monolayer thickness and surface functional groups change. How this change will influence the mechanical and fracture properties has not yet been answered and will be the main scope of this work.

The rest of this paper is arranged as follows. Section 2 introduces the methodology to determine the crystalline structures of Ti₃C₂-TiO₂ and validates its stability in silico. Subsequently, the mechanical properties of the Ti₃C₂-TiO₂ structures are explored through uniaxial tension in a ribbon model (Section 3) and a pre-crack model (Section 4). The variations in bond lengths and directions are employed to elucidate the strength and fracture processes of the Ti₃C₂-TiO₂ structures. Furthermore, the crack propagation process in the monolayer explains the larger cohesive zone and the unnoticeable anisotropy in these new structures. Section 5 closes this paper with discussions and conclusions.

2. Methodology

From our former works, pristine Ti₃C₂ structures were observed to be prone to oxidation [43]. When exposed to air conditions under room temperature, the adhesion force starts to decrease after 48 hours, as shown in Figure 1(a). Correspondingly, visible changes are found in the AFM images, indicating the initiation of oxidation and the formation of TiO₂ on the surface. Similar experimental results have also been reported to observe TiO₂ layers or nanoparticles deposited on the MXene surfaces [44, 45]. Currently, most of these observed TiO₂ are formed in the anatase phase, the interface between these two structures still lacks exploration and may have new unexplored stable crystal structures for Ti₃C₂-TiO₂ composites, as reported by Goel et al [46].

In this section, the crystal structures of Ti₃C₂-TiO₂ composites are constructed based on Molecular Dynamics (MD) and Density Functional Theory (DFT) methods. The mechanical and fracture properties of these crystal structures are then studied and discussed in the following sections.

2.1 Crystal structure of Ti₃C₂-TiO₂ composites

In this section, stable structures of Ti₃C₂-TiO₂ composite were successively identified using MD and DFT methods. The MD modeling is implemented with the Large-scale Atomic/Molecular Massively Parallel Simulator (LAMMPS) [47, 48]. The structure optimizations are obtained using the Vienna ab initio simulation package (VASP) [49] code based on DFT.

To find the stable crystal structure for Ti₃C₂-TiO₂, our initial step is to put two TiO₂ layers, adopting the crystal structure of rutile, on both sides of a fixed Ti₃C₂ substrate, series of cases with different relative locations between O atoms in TiO₂ and Ti atoms in Ti₃C₂ substrate were considered. Also, to overcome the lattice mismatch between these two structures, large sheets of TiO₂ and Ti₃C₂ structures created by duplicating unit cells were used for modeling while vacancies

were introduced along all directions so that the modeling box doesn't need to match the unit cell parameters. These combined structures are then stabilized using an NVT ensemble within LAMMPS for a total of 10 ps under a temperature of 10 K. The simulation uses real units with a timestep of 0.1 fs. The atom style is set to 'full', which means each atom can possess a charge, molecular type, and a full set of atomic properties. ReaxFF potentials are used to model the interactions between Ti, O, and C elements. QEq/Reax charge equilibration method is adopted using the fix charger command with a damping factor of 0.0 and a tolerance of 1.0×10^{-6} .

The stabilized structure obtained from this step is chaotic with all different combinations of Ti₃C₂ and TiO₂. From observation, we dig out several quasi-crystalline connections between Ti₃C₂ and TiO₂. Within these structures, the Ti₃C₂ part retains its initial structure while the TiO₂ part is transferred from the initial tetragonal structure of the rutile phase to a hexagonal structure like MXene. This transformation is mainly caused by the stress introduced by the lattice mismatch. These hexagonal TiO₂ structures are then applied to the whole Ti₃C₂ structure and stabilized again following the same unit cell and periodic setups. This process results in the formation of three distinct stable structures, adopting a sandwiched structure of TiO₂-Ti₃C₂-TiO₂. For all structures, the TiO₂ of both sides adopts similar structures while the bonds connecting TiO₂ layers with the Ti₃C₂ have different bond lengths and orientations. A total of two connection types were observed and named *bond-t*, which has bonds with lower angles with respect to the layer direction and the distance between the TiO₂ and Ti₃C₂ layers is relatively larger.

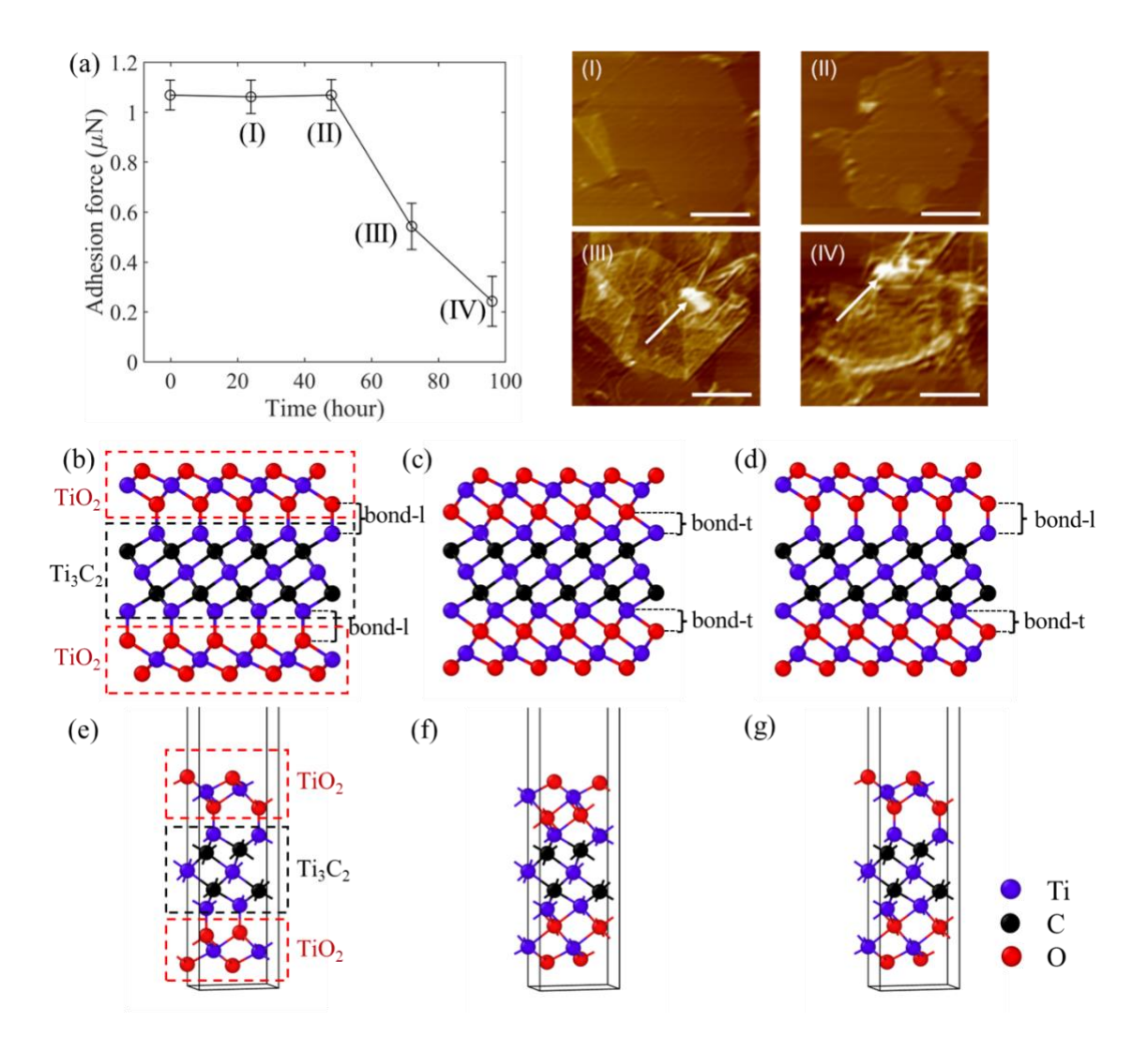


Figure 1. Adhesion force decay of exposure in the air for Ti_3C_2 flacks and corresponding AFM images. All scale bars are 1 μ m [43]. Side view of Ti_3C_2 - TiO_2 -Loose(b), Tight(c), Comb(d) structures. 3D view of Ti_3C_2 - TiO_2 -Loose(e), Tight(f), Comb(g) structures.

Adopting different combinations of these two connection types and depending on the distance between the TiO₂ layers and the Ti₃C₂, the three structures are named 'Loose', 'Tight', and 'Comb,' respectively, shown in Figure 1. In the Comb structure, the upper TiO₂ layer has a larger distance from Ti₃C₂, while the distance between the lower TiO₂ layer and Ti₃C₂ is low. Additionally, the TiO₂ layers in the formed structures are overall flat with small roughness along the z-direction, which is shown in Table S1 in Supplementary Information. This indicates a high

stability of the optimized composite structure. Afterward, to validate these stable crystal structures, we conducted DFT optimization on these three distinct stable structures. The Perdew-Burke-Ernzerhof (PBE) [50] version of the generalized gradient approximation (GGA) is employed to address the exchange-correlation energy of interacting electrons while the interaction between core and valence electrons in the simulations was modeled using the Projector Augmented-Wave (PAW) method. A plane wave cutoff energy of 600 eV is found to be appropriate to ensure that the forces are smaller than 10^{-2} eV/Å. The energy convergence threshold was set to 1×10^{-6} eV. Additionally, the EDIFFG parameter was set to -0.01 eV/Å, directing the simulation to continue until the forces acting on the atoms were reduced to less than 0.01 eV/Å. To rule out the interaction between isolated layers and confine our scope to single-layer scenarios, a vacuum spacing of at least 8 Å is introduced along the out-of-plane direction. The Brillouin zone in the DFT simulations was sampled using a Monkhorst-Pack grid, specified as $5\times5\times1$. The potential energies for the optimized unit cells of different Ti₃C₂-TiO₂ structures are close to each other with considerably small differences, which is approximately 0.17% of the potential of benchmark Ti₃C₂ MXene. This has been provided in Table S2 of the Supplementary Information along with the potential energy calculated using ReaxFF. For the same structures calculated using different approaches, the energy difference between ReaxFF and DFT ranges from 13% to 21%, primarily due to the differences in atomic layer spacing between the middle Ti₃C₂ layer and the TiO₂ layers of both sides.

The crystal structure cell parameters obtained using DFT and MD approaches were calculated and shown in Table 1, where the *a* and *b* are the in-plane cell parameters while the *h* refers to the monolayer thickness. The largest difference is only 1.87%, which indicates that the optimized structures using different algorithms match with each other. Detailed differences for the bond lengths and angles have also been analyzed and the results for the Comb structure are

illustrated in Figure 2(a). The errors mainly exist in lengths and angles for the bonds connecting the MXene and TiO₂ layers. Loose and Tight structures show similar trends.

Table 1 Unit cell parameters

Туре	a (Angstrom)			b (Angstrom)			h (Angstrom)		
	MD	DFT	Error	MD	DFT	Error	MD	DFT	Error
Loose	6.1730	6.2000	0.44%	5.3307	5.3696	0.73%	12.4063	12.6386	1.87%
Tight	6.0837	6.0572	0.44%	5.2021	5.24338	0.79%	12.1480	12.2204	0.60%
Comb	6.1866	6.1235	1.02%	5.2233	5.3035	1.54%	12.4298	12.4609	0.25%

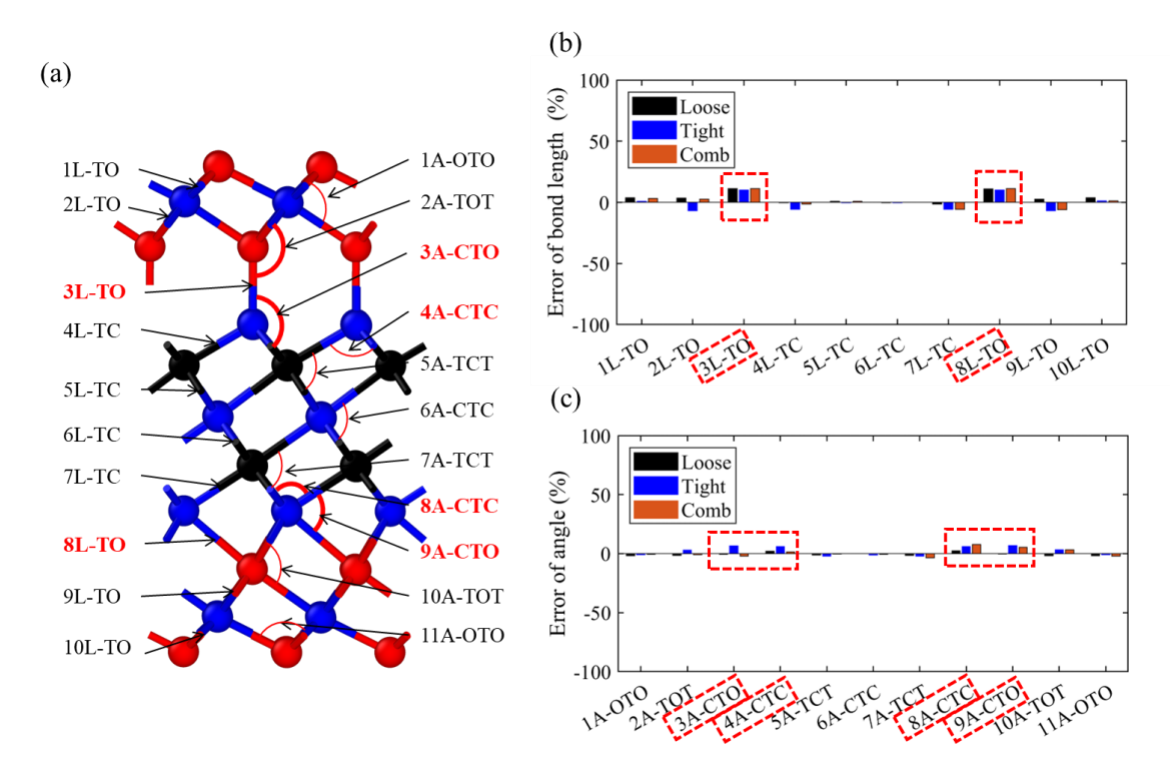


Figure 2. (a) Schematic diagram of bond lengths and angles of Comb structure. (b) Bond lengths of Loose, Tight, and Comb structures. (c) Angles of Loose, Tight, and Comb structures. 2.2 Molecular dynamics modeling setups.

In the preceding section, three stable Ti₃C₂-TiO₂ structures were identified. With the significant differences in atomic structure as well as the thickness due to variations in the TiO₂ structure on both sides, the mechanical and fracture mechanisms may also have distinct differences. To justify this inference, two types of models were established: nanoribbons and single-layer MXene with pre-cracks. The ribbon model provides a detailed explanation of the tensile characteristics of these three materials. For the pre-cracks model, tensile forces are applied to the mode-I crack model, investigating the cohesive zone and J-integral of different structures during the fracture process. Additionally, the fracture process of mode-mix involving changes in the tensile angle is also examined.

2.3 ReaxFF force field

Our work adopted the ReaxFF [48] aimed at modeling the atomic interaction of our new Ti₃C₂-TiO₂ structures. ReaxFF has been previously developed for MXene and metal oxides [51] and a variety of complex atom systems. It relies on a generic correlation between bond distance, bond order, and bond energy to ensure an accurate dissociation of both bonds and atoms.

3. Nanoribbon

3.1. Stress-strain responses

We established a series of uniaxial ribbon stretching models to investigate the impact of the stretching direction on the three structures of Ti₃C₂-TiO₂ structures. The structural dimensions are set to be 60 Å in length and 12 Å in width. Stretch deformation is conducted under NVT conditions at a temperature of 300K. One end is subjected to uniaxial tensile loading along the length direction with a velocity set at 0.001 Å /fs. The modeling results are shown in Figures 3-5.

In Figure 3(a), A and Z represent armchair and zigzag directions, respectively, while R denotes the nanoribbon. The three TiO₂ structures, Loose, Tight, and Comb, are abbreviated as L, T, and C, respectively.

3.1.1. Ti₃C₂-TiO₂-Loose structure

Figure 3(a) illustrates the stress-strain behavior during the tensile process of the Loose structure, with key stages of stretching as shown in Figure 3(b-e). For this and the following cases, we name the critical points on the stress-strain curves with the corresponding strain. For example, the ARL-2 point means the Loose nanoribbon loaded with a strain of 2 % along the armchair direction. In the armchair direction, during points 0 to 7, as strain increases, stress exhibits linear growth. In stages 7 to 12, a slight nonlinearity emerges, with a subtle decrease in slope. Correspondingly, when examining the bond situation, it is observed that within stages 0 to 12, there is no noticeable de-bonding within the ribbon's interior. On both sides of the ribbon, a small number of bonds break due to tension, as indicated by the red circles. After point 12, the ribbon rapidly undergoes a thorough fracture, leading to a sequence of unrecoverable debonding processes that leads to the initiation of overall fracture, as depicted in Figure 3(c).

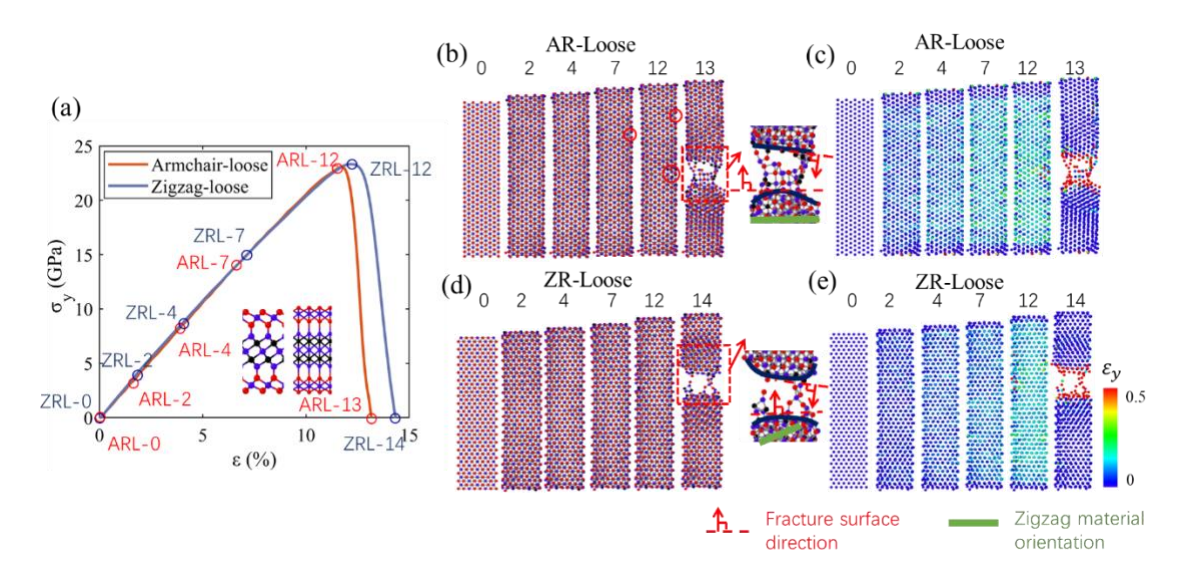


Figure 3. (a) Stress-strain response. (b and c) Bonding conditions and strain distribution for critical points of Ti₃C₂-TiO₂-Loose nanoribbon stretched along the armchair direction. (d and e) Bonding conditions and strain distribution for critical points of Ti₃C₂-TiO₂-Loose nanoribbon stretched along the zigzag direction.

Comparingly, from the stress-strain curve for zigzag direction as shown in Figure 3(a) as well as the corresponding structure change as shown in Figure 3(d-e), the stress-strain curve (ZRL) exhibits a similar evolution to that of the armchair direction. The distinction is in a larger strain at the point of fracture compared to the armchair direction. Observing the fracture surfaces, both directions display an arc-shaped cross-section, which significantly differs from the linear fracture surface observed in the tensile deformation of pure Ti₃C₂ ribbons [11]. Different from the obvious material orientation effects on pure MXene, the introduction of TiO₂ partially neutralized this influence. The fracture surface directions in both structures are mostly dominated by the loading conditions rather than the material orientations.

3.1.2. Ti₃C₂-TiO₂-Tight structure

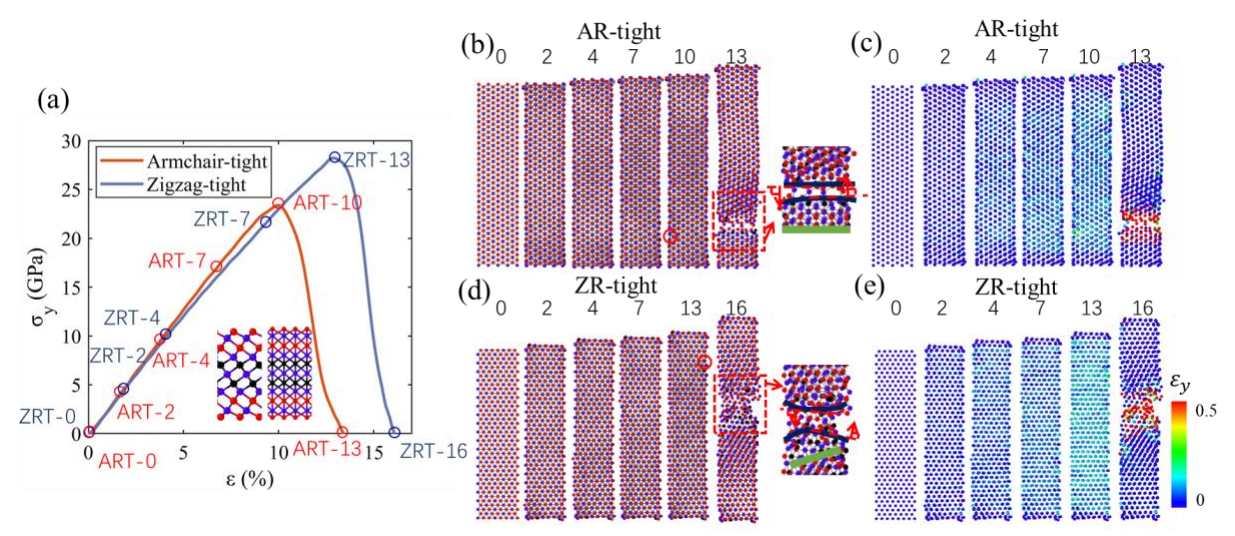


Figure 4. (a) Stress-strain response. (b and c) Bonding conditions and strain distribution for critical points of Ti₃C₂-TiO₂-Tight nanoribbon stretched along the armchair direction. (d and e) Bonding conditions and strain distribution for critical points of Ti₃C₂-TiO₂-Tight nanoribbon stretched along the zigzag direction.

The stress-strain curves of the Tight structures are like that of the Loose structure but with larger peak stress as well as corresponding strain. Another difference is shown in the difference between the peak stresses for different loading orientations. While the zigzag structures have larger strength than the armchair structures, the peak strength difference is much larger than that of Loose structures shown in Section 3.1.1. This may be caused by the compact structures with smaller distances between Ti₃C₂ and TiO₂ layers as in Tight structures, where the Ti₃C₂ and TiO₂ layers are more easily influenced by each other while deformed. Compared to the Loose structures, the larger distances between Ti₃C₂ and TiO₂ layers make them deform like three parallel semi-independent springs. This may explain why the strength of Tight structures is more correlated with the loading orientations. However, this influence is not reflected in the fracture surface orientations observed in Figure 4(c, e), which have small angles with direction perpendicular to the loading directions.

3.1.3. Ti₃C₂-TiO₂-Comb structure

The Comb structure is a combination of Loose and Tight configurations, with one side featuring TiO₂ layers in proximity and the other side having TiO₂ layers at a greater distance. Like the previous two structures, stress-strain responses possess tensile and fracture processes while exhibiting subtle nonlinearity before reaching peak stress. The peak stress in the armchair direction is close to the other two structures but with a higher fracture strain. For the structure loaded along the zigzag direction, the peak stress and fracture strain values are between those of the Loose and Tight structures. The tensile deformation in the armchair direction is shown in Figure 5(b). The crack angle is significantly less than 90 degrees, attributed to the asymmetry in TiO₂ layers on both sides of the Comb material.

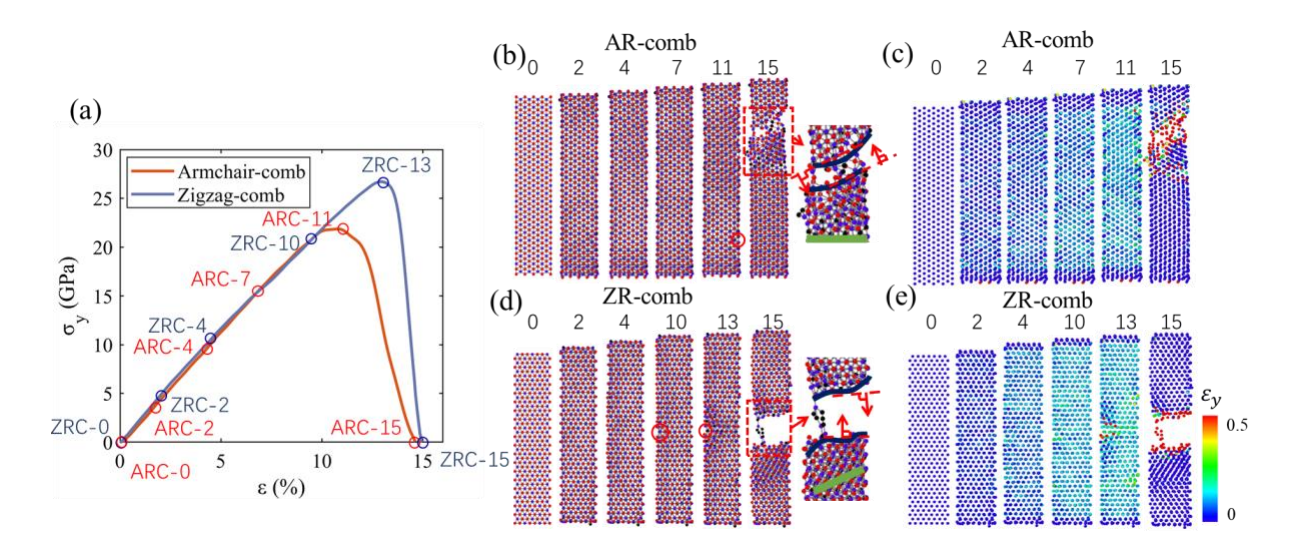


Figure 5 (a) Stress-strain response. (b and c) Bonding conditions and strain distribution for critical points of Ti₃C₂-TiO₂-Comb nanoribbon stretched along the armchair direction. (d and e) Bonding conditions and strain distribution for critical points of Ti₃C₂-TiO₂-Comb nanoribbon stretched along the zigzag direction.

For all these three structures, all fracture directions exhibit no distinct orientation effects during the uniaxial stretching. Rather than clean crack surfaces along the zigzag material orientations observed in uniaxial fracture observed in pure MXene structures[11], the introduction of TiO₂ layers has significant influences from two perspectives. First, the direction of the crack surfaces is more dominated by the direction of loading, rather than the direction of the material orientations, showing crack surfaces forming small and random angles with respect to the direction perpendicular to the loading direction. Second, the crack surfaces all display arc shapes rather than straight and clean surfaces. These two differences are all related to the highly active O atoms in the TiO₂ structures. While the debonding process, which usually starts from one side TiO₂ layer, will be illustrated in the following sections, the debonding processes of O atoms will lead to local structure reformation and change the stress distributions to align with the global loading conditions. From the images after fracture (Figures 3-5), the O atoms play important roles in the linkage

between two separated crack surfaces, showing as amorphous strings serving as connections. This bridging effect has also been observed and reported in former works [11].

Table 2 Mechanical and failure properties of Ti₃C₂ and Ti₃C₂-TiO₂ structures

		Loose	Tight	Comb	Ti ₃ C ₂
	Armchair	203.81	250.89	221.02	320.46
Young's modulus(GPa)	Zigzag	220.57	239.79	240.67	308.70
	Average	212.19	245.34	230.85	314.58
	Armchair	25.07	23.61	21.99	35.37
Peak stress(GPa)	Zigzag	23.36	28.18	26.75	37.99
	Average	24.215	25.895	24.37	36.68
	Armchair	316.88	288.51	273.33	168.71
Monolayer peak force (N-m)	Zigzag	295.27	344.36	332.50	181.21
(1.1.1)	Average	306.08	316.44	302.92	174.96
	Armchair	12.83	9.89	10.82	13.98
Peak strain(%)	Zigzag	12.23	13.02	12.95	16.29
	Average	12.53	11.455	11.89	15.14
	Armchair	15.57	13.29	14.63	17.21
Failure strain(%)	Zigzag	14.32	15.71	14.91	18.21
	Average	14.945	14.5	14.77	17.71

The mechanical and fracture properties of all three types of Ti₃C₂-TiO₂ structures are summarized and listed in Table 2. The Young's modulus of Tight structures is larger than that of Loose structures due to a more compact structure. For the peak stress, monolayer peak force (defined as the product of the peak stress and the monolayer thickness), peak strain (the strain corresponding to the peak stress), and failure strain (the strain corresponding to the point stress reaches zero), the Loose structure is larger along the armchair direction while the Tight structure triumphs along the zigzag direction, indicating material orientation effects on the mechanical and failure properties. Taking average values for comparison, the Tight structures are stiffer (larger

Young's modulus, peak stress, and monolayer peak force) while the Loose structures have a larger ductility (larger peak and failure strains). Comparing these Ti₃C₂-TiO₂ structures with pristine Ti₃C₂ MXenes, the addition of TiO₂ layers reduces Young's modulus and peak stress but increases the monolayer peak force due to a larger monolayer thickness.

3.1.4. Nonlinearity before fracture

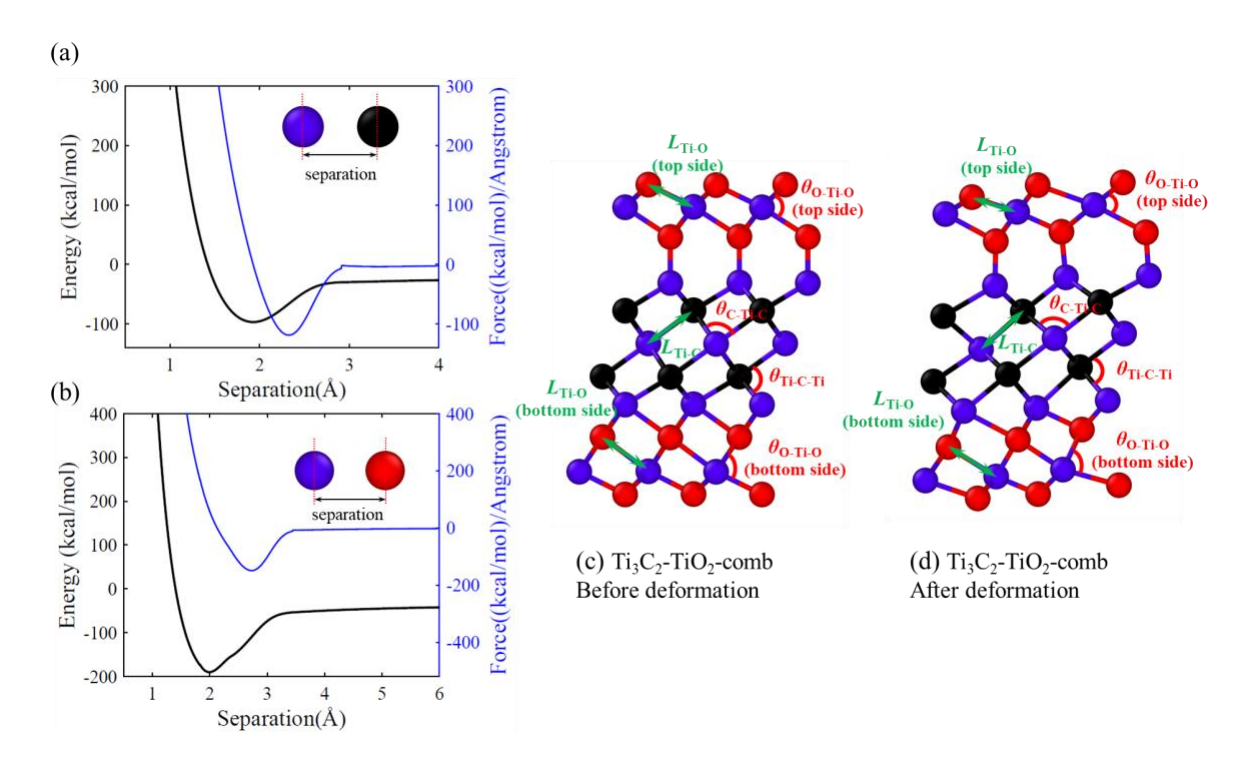


Figure 6. (a) Ti-C bonding energy and force versus separation. (b) Ti-O bonding energy and force versus separation. (c and d) Bond length and bonding angles definition.

To explain the nonlinearities before fracture, for the stage before the peak stress is reached, (shown as the strain between 2% and 12% as in Figures 3-5), we studied how the structure deformation is correlated with the stress-strain responses using seven key parameters (three bond lengths and four angles) for representation and quantitative analysis: Ti-C bond length, Ti-O bond length (top and bottom side), C-Ti-C angles, Ti-C-Ti angles, and O-Ti-O angles (top and bottom

side). Taking the Comb structure as an example, the definitions of bond lengths and angles are shown in Figure 6. The change of the bond lengths is compared with the trend of stress-strain responses and shown in Figures 7-8.

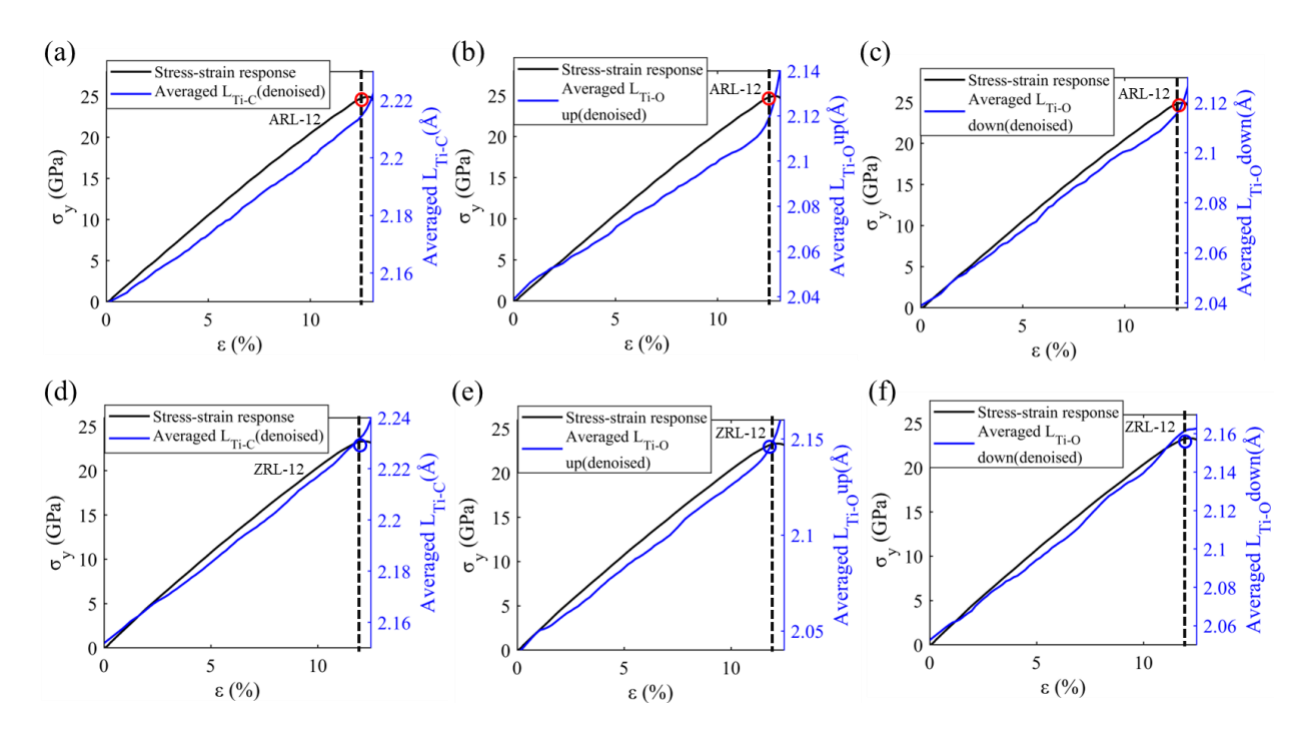


Figure 7. (a–c) L_{Ti-O} (top side), L_{Ti-C} , L_{Ti-O} (bottom side) regarding strain for Ti_3C_2 - TiO_2 -Loose nanoribbon stretched along the armchair direction. (d-f) L_{Ti-O} (top side), L_{Ti-C} , L_{Ti-O} (bottom side) regarding strain for Ti_3C_2 - TiO_2 -Loose nanoribbon stretched along zigzag direction.

The bond length variations in the Loose and Tight structure are shown in Figures 7-8. From the stress-strain responses, two stages could be found that are separated by the dashed line: the quasi-linear stage where stress increases quasi-linearly with strain, and the non-linear stage. Starting from strain 0%, the trend of all bond lengths is consistent with stress, exhibiting a nearly monotonic increase with strain. After the maximum stress, the slope starts to gradually decrease, and both the bond length and stress-strain curves enter a nonlinear phase accordingly. The bond lengths change either more rapidly or slowly while the angles could even change from decreasing

to increasing for several angle definitions (Figures S1-S2 of Supplementary Information). These changes are reflected as changing slopes in the stress-strain curves in this stage.

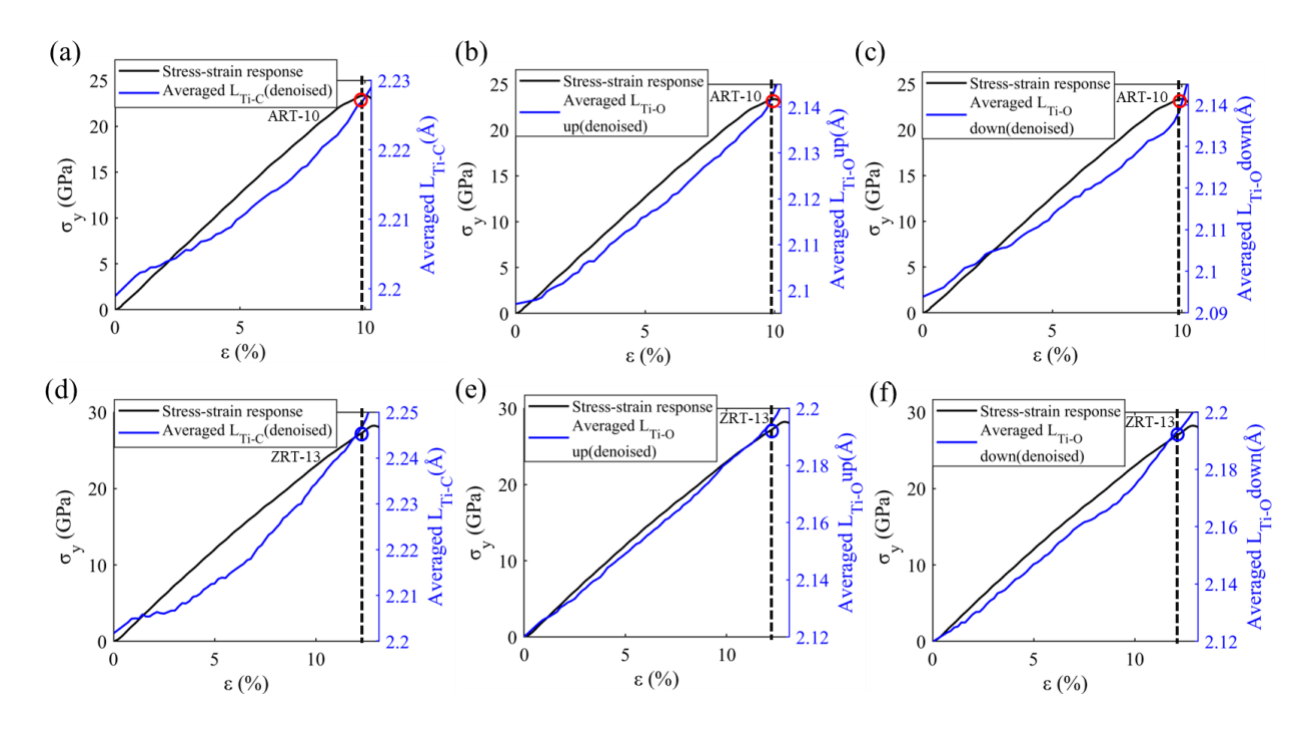


Figure 8. (a–c) L_{Ti-O} (top side), L_{Ti-O} (bottom side) regarding strain for Ti_3C_2 - TiO_2 -Tight nanoribbon stretched along the armchair direction. (d-f) L_{Ti-O} (top side), L_{Ti-C} , L_{Ti-O} (bottom side) regarding strain for Ti_3C_2 - TiO_2 -Tight nanoribbon stretched along zigzag direction.

The overall trends in structural changes for the Comb structures are like those of Loose and Tight (Figures S3-S4 of Supplementary Information). A notable difference is the significant nonlinearity in bond lengths for Tight between strain 0% and 13%, with Comb showing a slightly lower level of nonlinearity. The primary cause of this nonlinearity is the proximity of TiO₂ layers. Clearly, the name "Loose" is assigned to the wider distance between the TiO₂ layers and Ti₃C₂, which exerts a suppressed effect on the structure's nonlinearity. Consequently, the interaction with MXene, i.e., Ti₃C₂, is weaker, resulting in minimal nonlinearity in bond lengths. In contrast, both sides of the Tight structure have TiO₂ layers near Ti₃C₂, leading to substantial nonlinearity in bond

lengths. The Comb structure features TiO₂ layers on both sides, with one side having proximity and the other having a greater distance, resulting in the nonlinearity in bond lengths that fall between that of the Loose and Tight structures.

3.2. Fracture

To have a more detailed and illustrative concept of how each of these Ti₃C₂-TiO₂ structures fails, we extracted the debonding process for each structure and showed it in a 2D representative plane. The corresponding processes are shown in Figures 9-11.

3.2.1. Ti₃C₂-TiO₂-Loose structure

From Figure 9, it is shown that the de-bonding processes in both loading directions initiate from the TiO₂ layer of one side while the Ti₃C₂ layer and the TiO₂ layer of the other side remain intact. In the armchair structure, the fracture initiates from the upper TiO₂ layer and then propagates to the Ti₃C₂ layer. It is worth noting that the debonding happens to the bonds with a smaller angle with respect to the loading directions, which will bear a larger portion of force while deformed. Afterward, the Ti₃C₂ MXene layer breaks before the lower TiO₂ layer. After the initial fracture of the upper TiO₂ layer, MXene's initially symmetric structure transformed into an unsymmetric one, and the loading conditions turned eccentric. The remaining Ti₃C₂ and lower side TiO₂ layers bend to reach new balance conditions, creating a bending scenario where the Ti₃C₂ is under tension and TiO₂ under compression. This leads to a higher force on the Ti₃C₂ MXene and furthermore fracture. Subsequently, the lower TiO₂ layer, bearing a greater force due to the smaller angle of several parallel bonds with the loading direction, new fractures developed from the bottom

and pointed upward. Ultimately, the fractures from both directions converge, leading to complete penetration fracture.

In the zigzag direction, the de-bonding process is similar to that of the armchair direction. The fracture initiated from one side of the TiO₂ layers and subsequently, the MXene, subjected to a higher bending moment, undergoes fracture. Finally, the TiO₂ layer on the other side fractures, resulting in a complete penetration fracture across the cross-section.

TiO₂ layers of both sides connect to the Ti₃C₂ MXene layer through Ti-O bonds. In the Loose structures, the orientation of these bonds is perpendicular to the loading directions, which means that these bonds serve only connection purposes and do not take force while deformed. Accordingly, almost no connecting bonds are observed to be broken during the whole process. In this manner, the deformation and fracture processes of the TiO₂ layers and Ti₃C₂ layer are almost independent of each other. The whole structure deformation is similar to that of three parallel springs with weak connections.

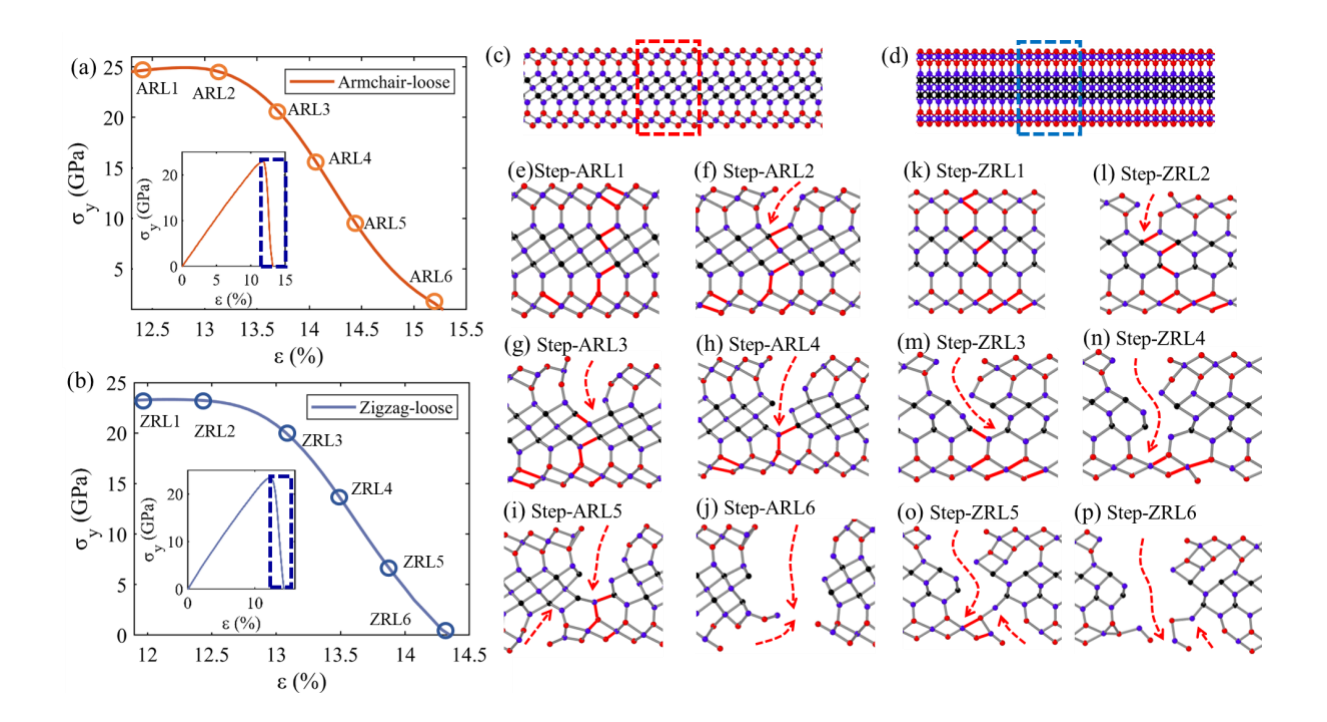


Figure 9. (a and b) Critical points for descending stage of Ti₃C₂-TiO₂-Loose nanoribbon stretched along armchair and zigzag directions. Side view for Ti₃C₂-TiO₂-Loose nanoribbon loaded along (c) armchair and (d) zigzag direction. De-bonding process for Ti₃C₂-TiO₂-Loose nanoribbon stretched along (e–j) armchair and (k–p) zigzag direction. 3.2.2. Ti₃C₂-TiO₂-Tight structure

In the Tight structure, the fracture also occurs at one outer TiO₂ layer. In contrast to the Comb structure, the orientation of Ti-O bonds in the armchair direction at the interface in the Tight structure is different, forming acute angles with the loading direction. This results in higher stress on the Ti-O bonds at the interface, leading to the fracture of all Ti-O bonds in the interface. The fracture initiates from one side of the TiO₂ layer, where the parallel bonds (including Ti-O bonds between the upper TiO₂ layer and Ti₃C₂) with a smaller angle to the loading direction bear a greater load and are consequently more susceptible to fracture. Consequently, these parallel bonds break first, penetrating into the inner Ti₃C₂ layer, and subsequently, the TiO₂ layer (with similar parallel bonds) on the other side undergoes de-bonding, resulting in a complete penetration fracture.

In the Zigzag direction, the upper TiO₂ layer exhibits a clear parallel orientation with the upper Ti₃C₂ structure, and these bonds have a small angle with the loading direction. The debonding process precisely initiates from these parallel bonds, as depicted in Figure 10(k-m). Subsequently, the fracture progresses from the Ti₃C₂ layer penetrating down to the lower TiO₂ layer, resulting in complete fracture. Throughout this process, the bonds between the lower TiO₂ and Ti₃C₂ do not break because the connecting bonds are perpendicular to the loading directions.

In structures involving both directions, the bonds connecting the TiO₂ layers to Ti₃C₂ exhibit acute angles with the stretching direction. These bonds not only serve as a connecting function but also bear the tensile load.

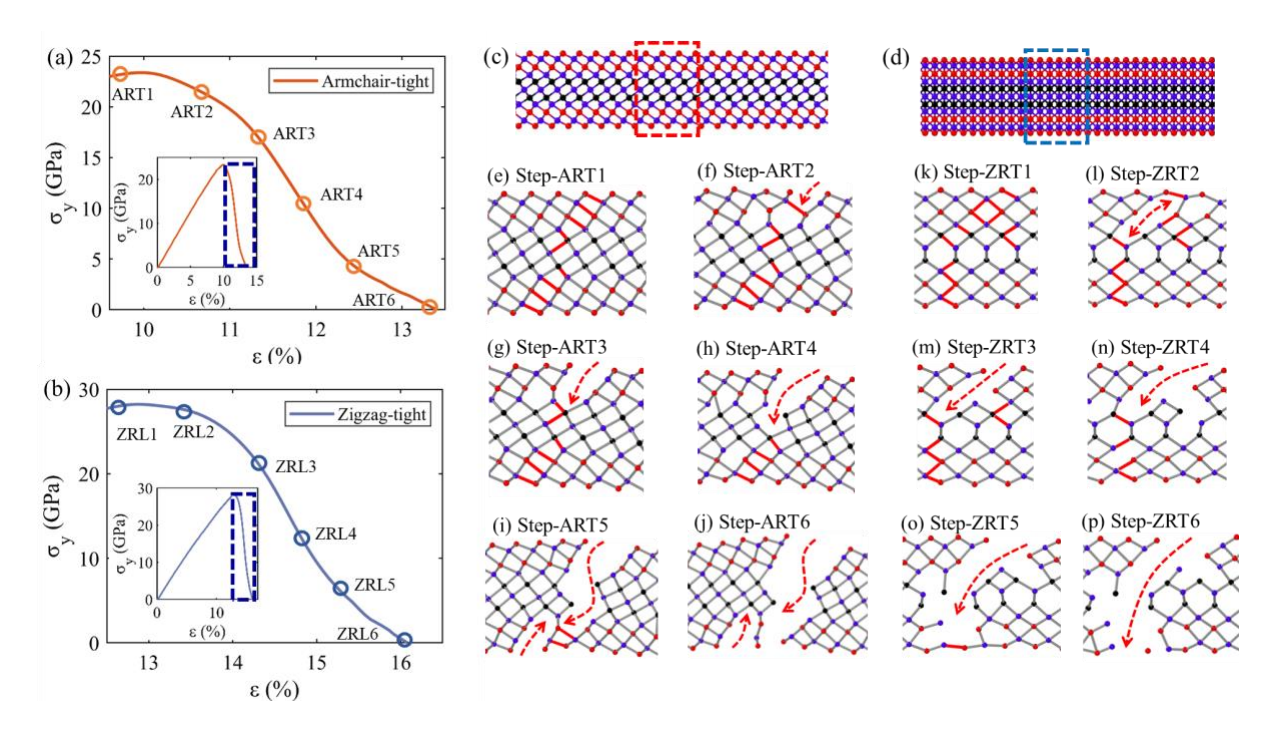


Figure 10. (a and b) Critical points for descending stage of Ti₃C₂-TiO₂-Tight nanoribbon stretched along armchair and zigzag directions. Side view for Ti₃C₂-TiO₂-Tight nanoribbon loaded along (c) armchair and (d) zigzag direction. De-bonding process for Ti₃C₂-TiO₂-Tight nanoribbon stretched along (e–j) armchair and (k–p) zigzag direction.

3.2.3. Ti₃C₂-TiO₂-Comb structure

From the first two structures (Loose and Tight), we can observe that the de-bonding process is more likely to initiate from several parallel bonds, which are at an acute angle with the stretch direction. This makes it easy to explain the fracture process in the Comb structure. As shown in Figure 11(e-g), for armchair direction, the lower TiO₂ layer exhibits numerous parallel bonds with the underlying Ti₃C₂ structure. Consequently, fracture initiates from the bottom and gradually penetrates upward. In the armchair direction, the fracture initiates from the bottom and gradually penetrates upward, resulting in an inclined cross-section. Along the zigzag direction, however, there are no clearly defined parallel bonds with a small angle relative to the loading direction. The fracture occurs randomly from one side to the other, resulting in a perpendicular cross-section.

Throughout the entire process of fracture along the armchair direction, the bonds between the upper TiO_2 layer and Ti_3C_2 do not break. However, the bonds between the lower TiO_2 layer and Ti_3C_2 not only serve as connectors but also actively participate in bearing the tensile forces in the loading direction. This pattern is also evident in the zigzag direction.

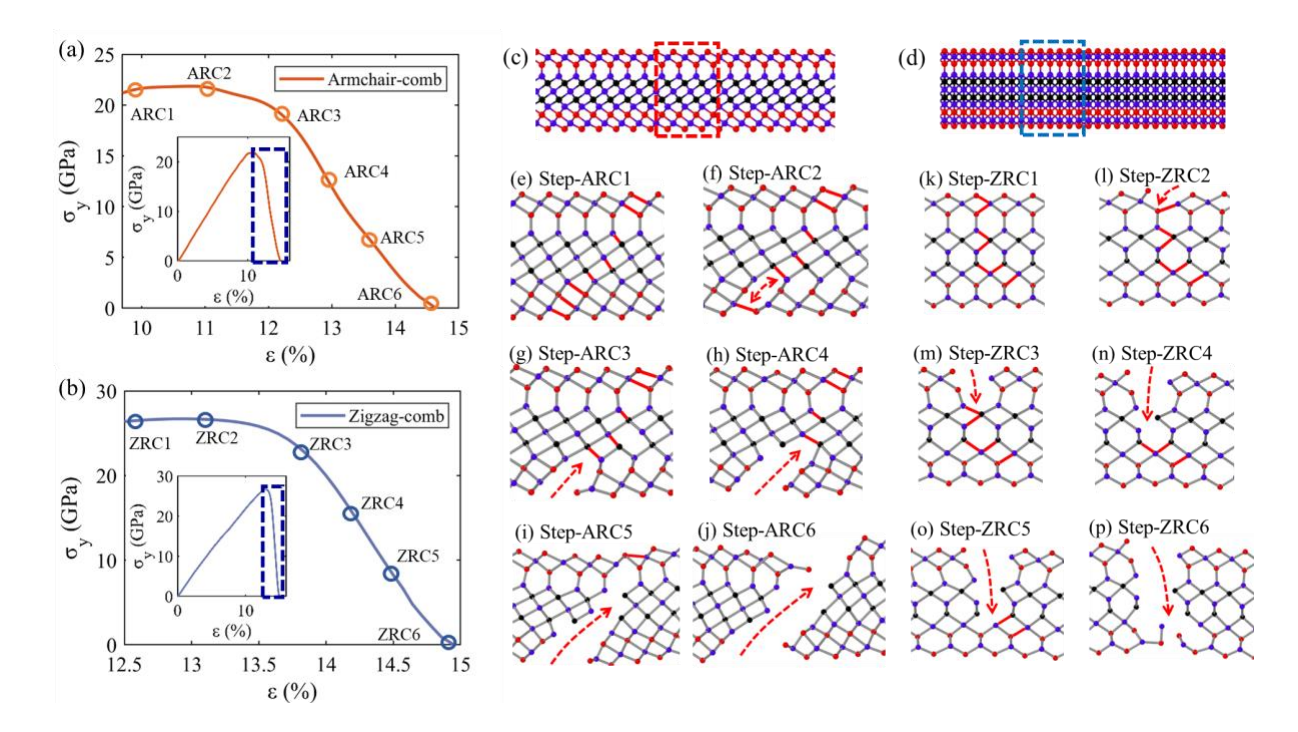


Figure 11. (a and b) Critical points for the descending stage of Ti₃C₂-TiO₂-Comb nanoribbon stretched along armchair and zigzag directions. Side view for Ti₃C₂-TiO₂-Comb nanoribbon loaded along (c) armchair and (d) zigzag direction. De-bonding process for Ti₃C₂-TiO₂-Comb nanoribbon stretched along (e–j) armchair and (k–p) zigzag direction.

4. Pre-cracked monolayer

This chapter investigates the fracture behaviors of monolayer Ti₃C₂-TiO₂ structures with pre-existing cracks. The pre-crack, loading conditions, and dimensional setups are shown in Figure 12(a), with a model size of 90Å×112Å. The primary differences among the three structures lie in their thickness, resulting from variations in the spacing of the TiO₂ layer arrangement. The pre-cracked models of Loose, Tight, and Comb structures in the armchair and zigzag directions are

shown in Figure 12(b). The fracture behavior is characterized using the cohesive zone and J integral methods. The definitions employed are consistent with those found in the papers. The length of the cohesive zone is defined by the distance between the zero-stress point and the peak stress. Simultaneously, the length of the zero-stress region is referred to as Δa , as shown in Figure 12(d). The J integral method utilizes an atomic-scale definition. In this model, the selected atomic region for calculation is depicted in Figure 12(c).

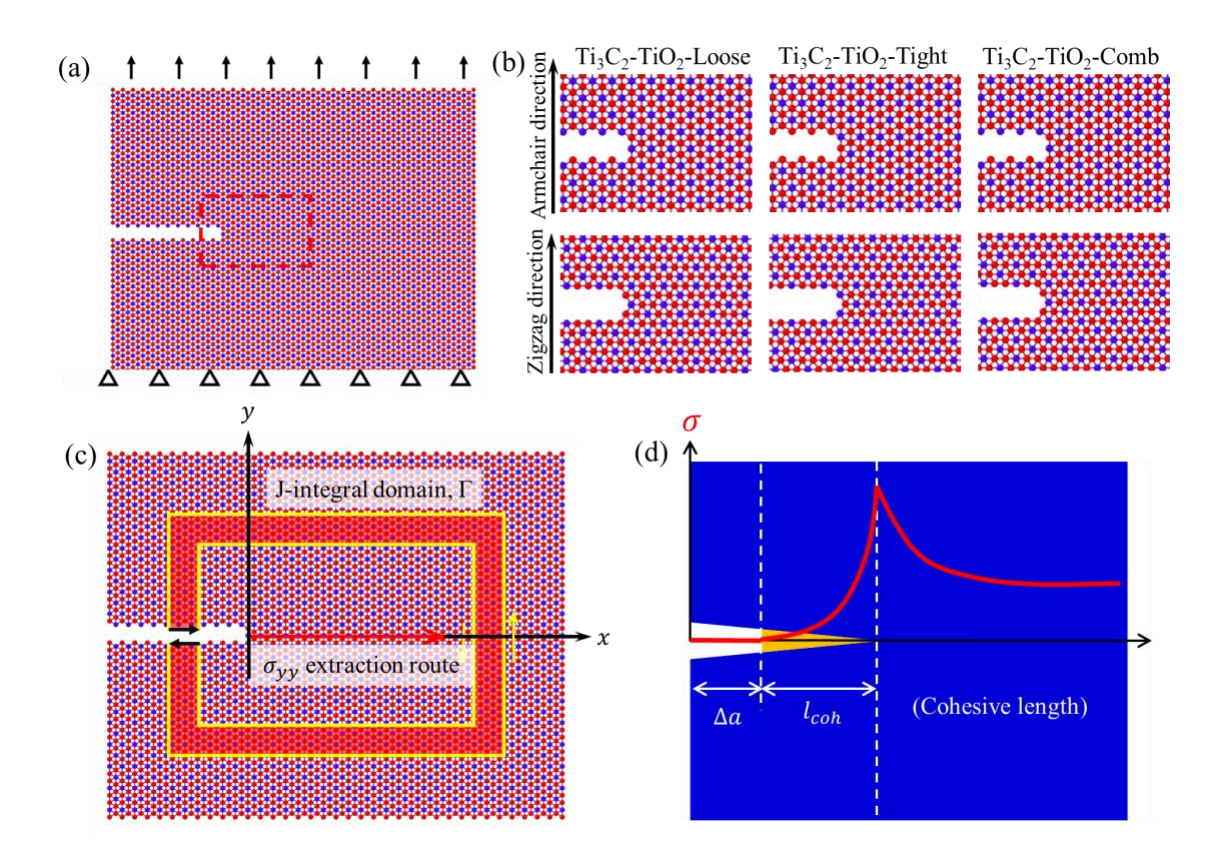


Figure 12. (a) Modeling setup for monolayer MXene. (b) Pre-crack tip for Ti₃C₂-TiO₂-Loose, Tight, and Comb of both directions. (c) σ_{yy} extraction route and integration domain for J-integral calculation. (d) Δa and l_{coh} definition.

4.1. Mode-I fracture

4.1.1. Ti₃C₂-TiO₂-Loose structure

describing a specific state: before crack initiation, at the moment of crack initiation where the atoms at the crack tip just de-bond, resulting in zero stress at the tip, and after the crack has propagated to a certain extent with a newly formed complete crack length denoted as Δa . In the first step, the peak stress occurs at the position of the crack tip, with stress decreasing along the pre-crack direction and subsequently leveling off. As the crack tip atoms start to de-bond, the crack initiates. With the crack propagation, the maximum stress point shifts to the right, moving to the new crack tip, as shown in step 2. Simultaneously, the stress around the pre-crack diminishes until reaching zero, this is shown as a cohesive zone where the initial structure fails but the newly generated surfaces relate to amorphous Ti-C-O structures. The thickness of cohesive zones grows lower with the loading process. As the crack further extends, the initially generated cohesive zone around the original crack tip breaks entirely and the stress decreases to around zero, here referred to as zero-stress range Δa . The stress distribution in Step 3 around the moving crack tip follows the same pattern as the previous step but in different locations. As the crack propagates deeper, the corresponding zero-stress range Δa increases. However, the peak stress and cohesive zone length in Step 3 are almost the same as those in Step 2.

In the process of fracture, three representative points are shown in Figure 13, each

From the stress distribution shown in Figure 13(a) at the atomic level, peak stress is located at the crack tip where the bonds between atoms remain intact, corresponding to the Γ_0 point in the J integral shown in Figure 13(b). This value then increases until reaching Γ_s , indicating the complete formation of an entire cohesive zone before the new crack tip. The difference between these two values reveals the nonlinearity that is introduced by the addition of TiO₂, which is

notably greater than that of Ti₃C₂ MXene. This also shows in a larger area of cohesive zone. The Zigzag direction exhibits a similar trend and is shown in Figures S5-S7 of Supplementary Information.

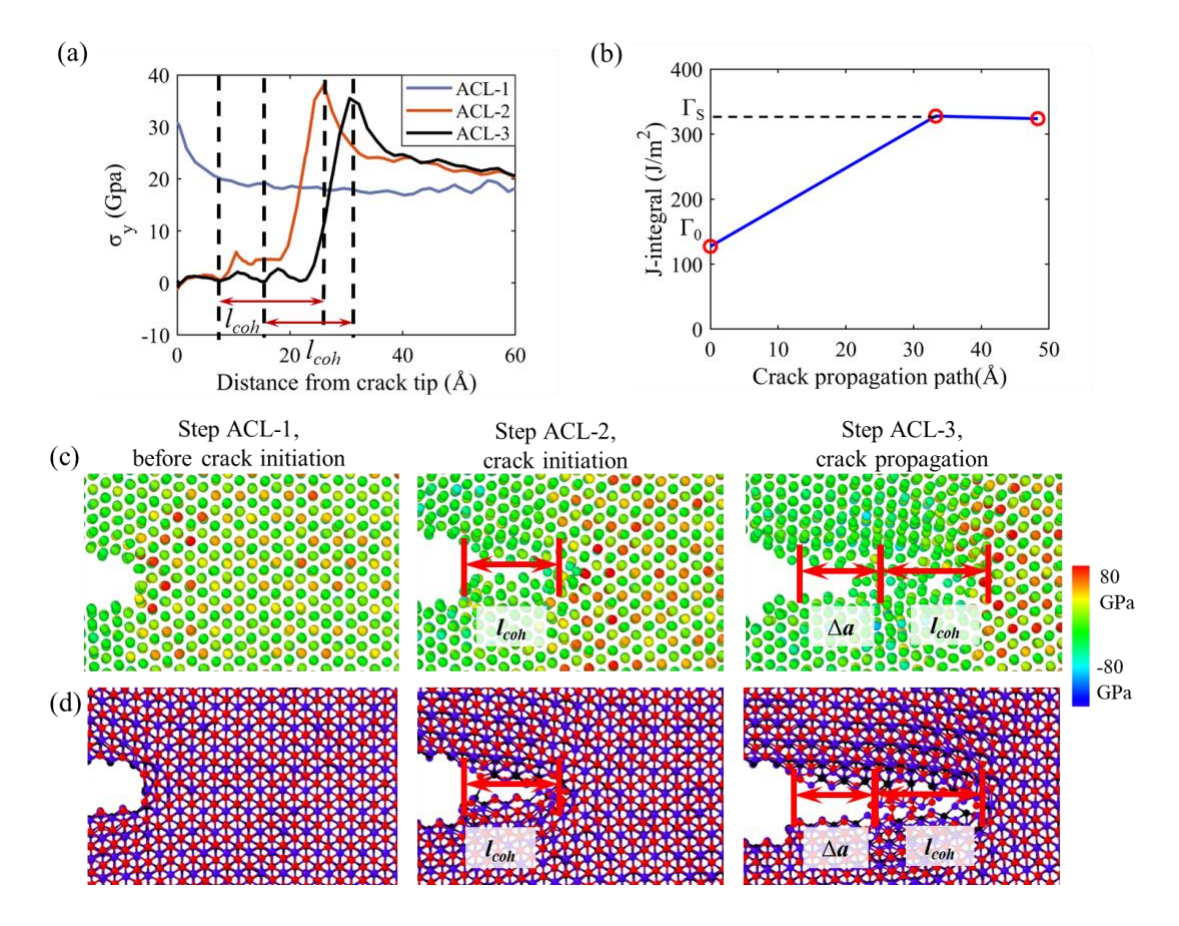


Figure 13. Pre-cracked monolayer Ti_3C_2 - TiO_2 -Loose structure stretched along the armchair direction. (a) σ_{yy} along crack extension direction for different steps. (b) J integral versus crack propagation path. (c) Stress distribution of crack tip area for different steps. (d) Bonding conditions of crack tip area for different steps.

4.1.2. Ti₃C₂-TiO₂-Tight structure

Figure 14 shows the structure as well as the stress distribution change of the Tight structure fracture processes along the armchair direction, which shares similarities with the patterns observed in Loose structure cases. It undergoes initial stress concentration at the crack tip with

intact bonds, and then the stress concentration shifts to the new crack tip as the crack propagates, with the fully fractured length denoted as Δa . Cohesive zones are also observed to have the same level of lengths and peak stresses alike the Loose structure cases.

The cohesive zone lengths for Tight structures are at the same level but higher than that of Loose structure cases. When the bonds at the tip atoms begin to break (Step 2, 3), the stress at the far end of the crack propagation direction (approximately constant) is also higher in Tight structure. This is because the bond direction between TiO₂ layers and MXene has a smaller angle with the stretch direction in the Tight structure, providing the overall structure with higher strength. In contrast, the bond angle in Loose is nearly perpendicular to the stretch direction, resulting in minimal contribution to load bearing.

As for the J-integral shown in Figure 14(b), the major difference is observed in the value difference between Γ_s and Γ_0 , which is lower than that obtained in the Loose structure cases. This indicates a lower level of nonlinearity caused by the more compact structure where the TiO₂ layers are closer to the Ti₃C₂ layer. This is also revealed in the cohesive zone shown in Figure 14(c-d), where the length is at the same level with Loose structure cases, but the molecular structures observed in the cohesive zone are much less chaotic. The Zigzag structures are shown in Figures S5-S7 in Supplementary Information.

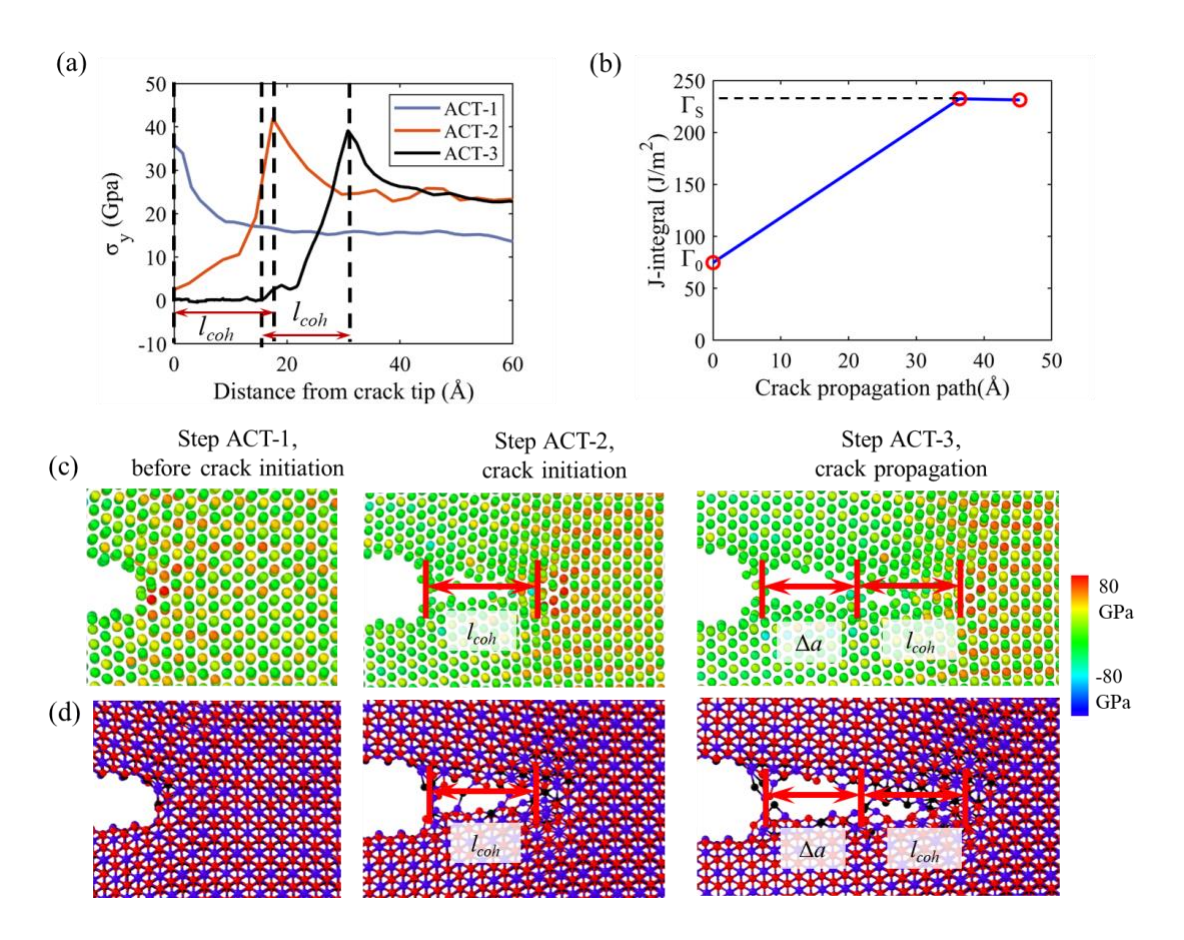


Figure 14. Pre-cracked monolayer Ti_3C_2 - TiO_2 -Tight structure stretched along the armchair direction. (a) σ_{yy} along crack extension direction for different steps. (b) J integral versus crack propagation path. (c) Stress distribution of crack tip area for different steps. (d) Bonding conditions of crack tip area for different steps.

4.1.3. Ti₃C₂-TiO₂-Comb structure

The Comb structure, as indicated by the distribution of TiO₂, is a combination of Tight and Loose structures, featuring one side with a larger spacing of TiO₂ layers and the other side with a smaller spacing. This asymmetry results in notable differences in Steps 1, 2, and 3 compared to the first two structures. As shown in Figure 15(a), after the de-bonding of tip atoms in the precrack, the cohesive zone gradually expands, and there is no clearly defined zero-stress region, as observed in the previous two structures. Additionally, Figure 15(a) reveals significant low-stress fluctuations within the cohesive zone. The difference in J integral ($\Gamma_s - \Gamma_0$) is in between that of

the Tight and Loose structure cases but closer to the Tight structure case, indicating relatively low nonlinearity.

In the case of stretch deformation along the zigzag direction, the cohesive zone exhibits characteristics similar to those in the armchair direction, gradually expanding. However, from the J integral shown in Figure 15(b), it is evident that nonlinearity is maximized. It is important to note that the cohesive zone in both directions shows a gradual expansion trend. Due to the model length considerations, the exact extent to which the cohesive zone can develop is not the focus of this study.

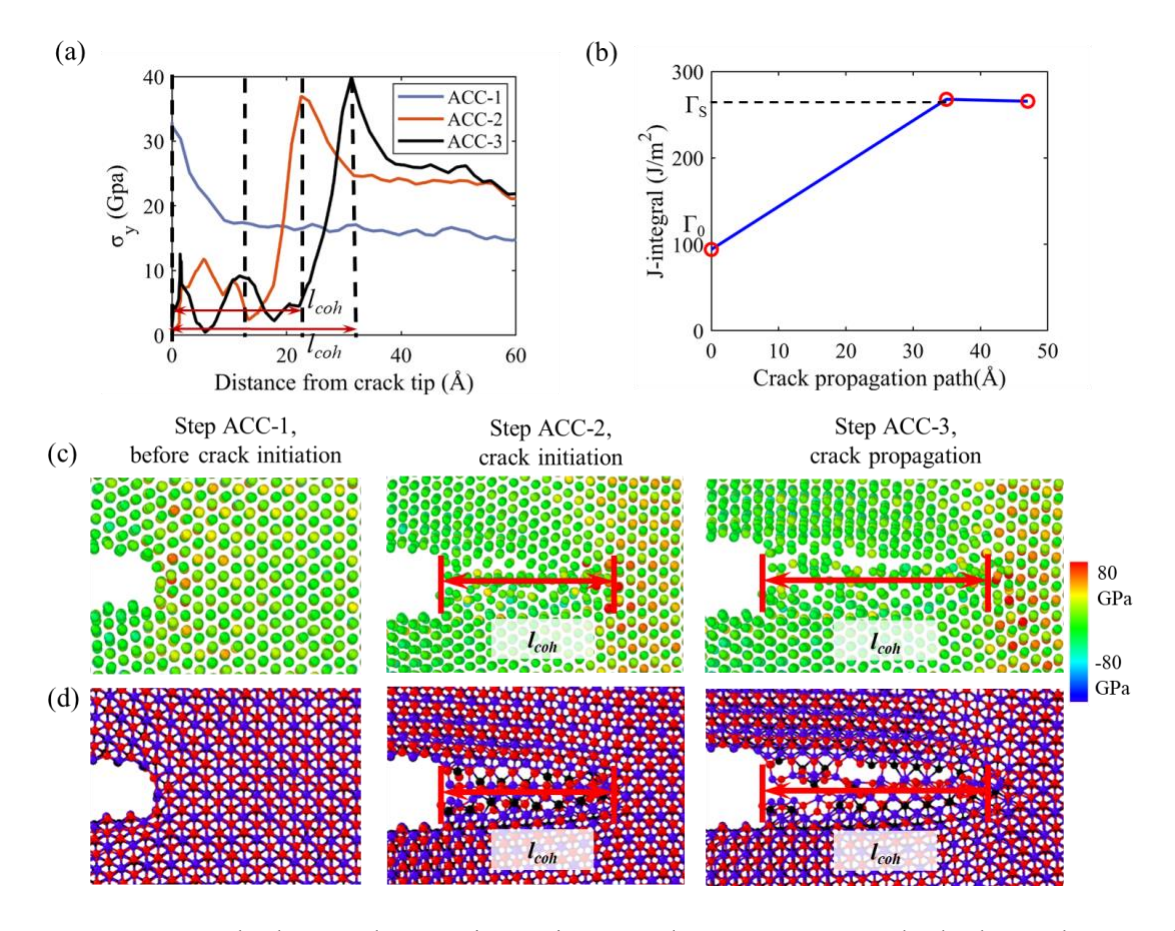


Figure 15. Pre-cracked monolayer Ti_3C_2 - TiO_2 -Comb structure stretched along the armchair direction. (a) σ_{yy} along crack extension direction for different steps. (b) J integral versus crack propagation path. (c) Stress distribution of crack tip area for different steps. (d) Bonding conditions of crack tip area for different steps.

4.1.4. Toughness

Figures 16-18 depict the size of the cohesive zones and toughness (Γ_s) for all structures. Compared to the other two structures, the thickness of the Loose structure is the greatest, but its cohesive zone is the lowest in both stretch directions. The Comb structure case has the largest cohesive zone sizes along both directions, which is caused by the asymmetric nature. For all structures, the cohesive zone lengths along the armchair direction are larger than the zigzag loading cases, showing the material orientation effect on the final fracture. As for the toughness of all the armchair cases, the Loose structure case has a larger value compared with the Tight structure case. However, it is larger for Tight structure cases when it comes to the loading along zigzag directions. For both loading directions, the toughness of the Comb structure case is in between that of Tight and Loose structures, which is reasonable since it is a combination of these two structures.

From the side view of the crack tip area with cohesive zones covered with surface meshing shown in Figures 17-18, a significant thinning effect is observed at the cohesive zones where the thickness shrinks by approximately 50% for each case.

Another thing to notice is the crack propagation directions. In our former work, pristine MXene adopts strong material effects when loaded along different material orientations. With the introduction of TiO₂ structures, for all Tight, Loose, and Comb structures, the crack propagation direction is all along the pre-crack extension direction, which is also perpendicular to the loading directions. This behavior is more often observed in homogeneous materials rather than anisotropic 2D materials. The highly active O atoms play important roles in the local reformation when debonding processes start, which leads to the loading condition-dominated fractures observed in all Ti₃C₂-TiO₂ structures.

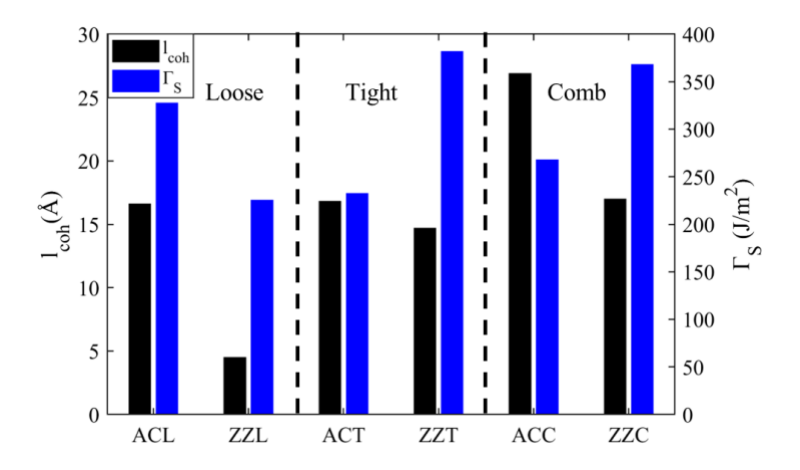


Figure 16. *l_{coh}* and fracture toughness for all structures.

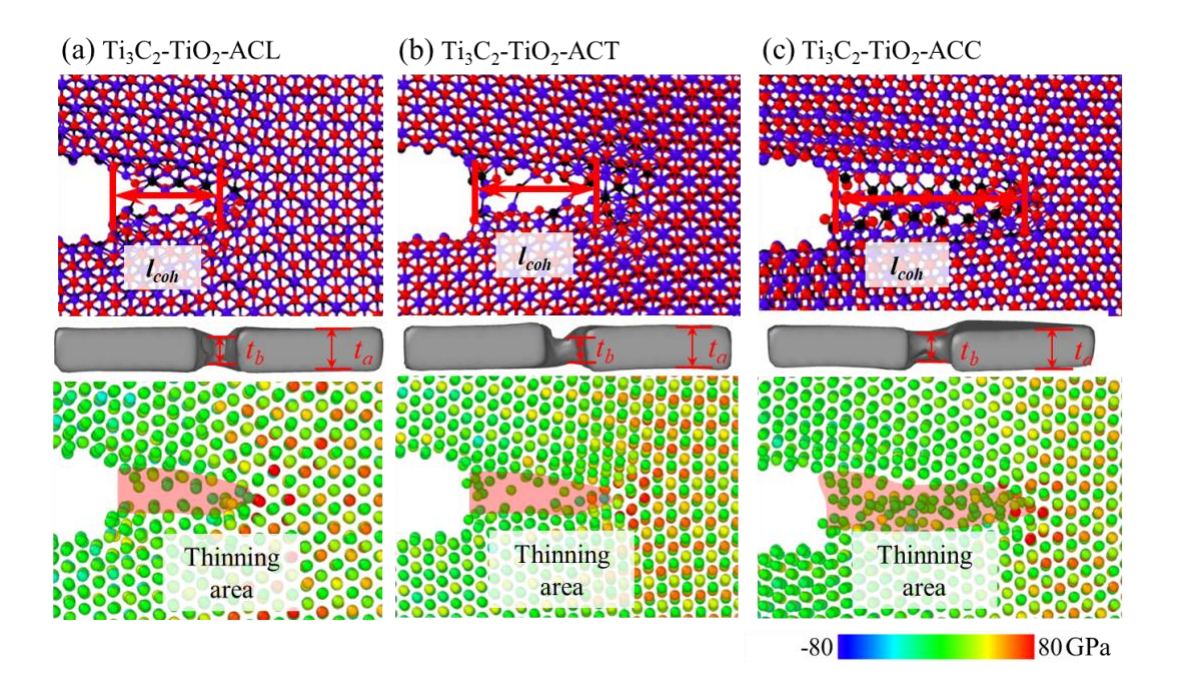


Figure 17. Bonding conditions, crack tip thickness, and σ_{yy} distribution of crack initiation step for (a) Loose, (b) Tight, (c) Comb structures along armchair direction.

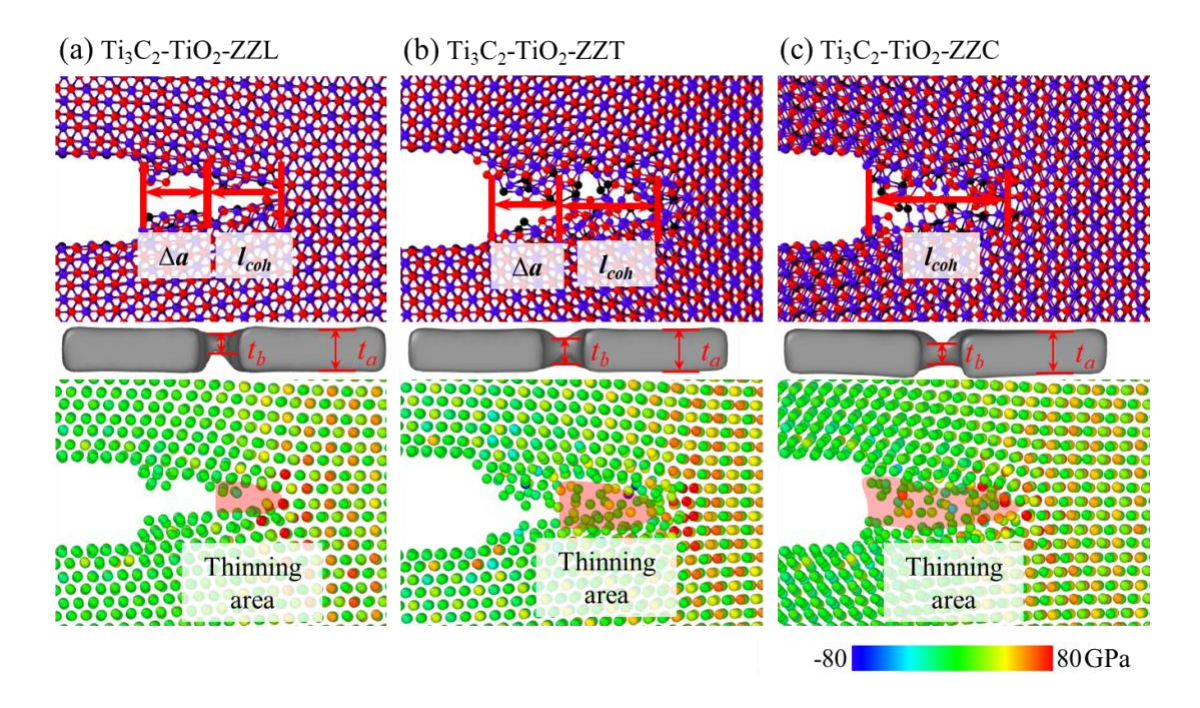


Figure 18. Bonding conditions, crack tip thickness, and σ_{yy} distribution of crack initiation step for (a) Loose, (b) Tight, and (c) Comb structures along zigzag direction.

4.2. Mode-mix fracture

The crack propagation direction as well as the toughness change with respect to the load direction under mode-mix loading conditions are also explored in this work. The loading angle is defined as the angle between the crack propagation and the direction perpendicular to the uniaxial loading direction, shown as θ as in Figure 19. The crack bifurcation angle (α) as well as cohesive zone length l_{coh} are also used for quantitative analysis. The loading angle θ , which is defined as the angle with respect to the mode-1 loading direction, is set to have values of 15, 30, 45, 60, and 75 degrees, respectively.

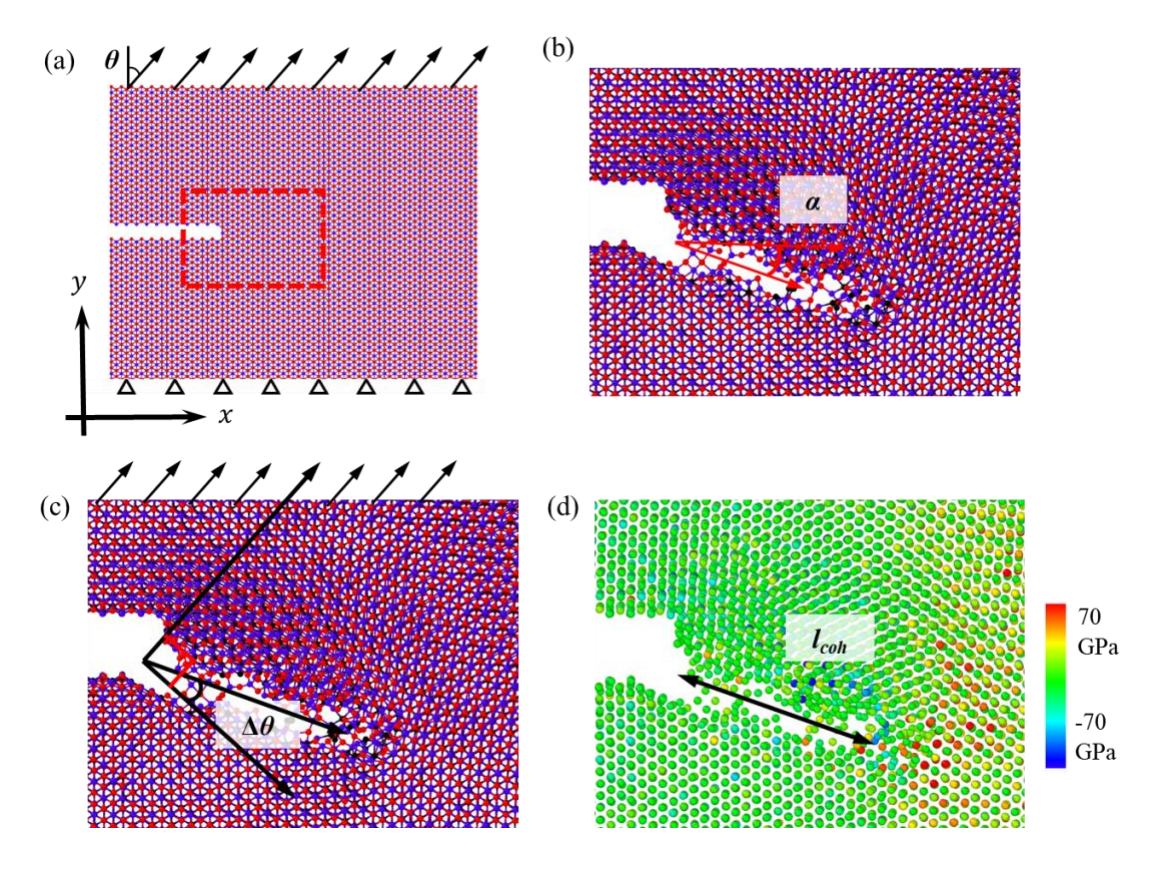


Figure 19. (a) Modeling setup for mode-mix fracture of monolayer TiO_2 - Ti_3C_2 - TiO_2 structure. θ is the loading angle regarding strain. (b) Crack propagation angle (α) definition with TiO_2 - Ti_3C_2 - TiO_2 loaded with an angle of 45-deg. (c) $\Delta\theta$ definition with TiO_2 - Ti_3C_2 - TiO_2 loaded with an angle of 45 deg. (d) l_{coh} for mode-mix fracture.

The traction components across discontinuity for two-dimensional cases, experience Mode I tension traction (σ_{0n}) and Mode II shear traction (σ_{0t}) (Figure 20).

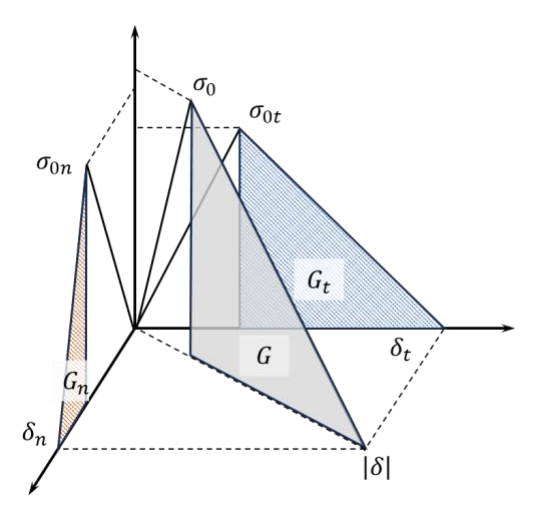


Figure 20. Fracture energy dissipated based on a traction-separation curve.

The modeling results for each structure can be found in the Supplementary Information. To study how the loading conditions influence the overall behavior, we extracted the $\sigma_{0t} - \sigma_{nt}$ and $G_n - G_t$ relationships for all structures as shown in Figure 21 to illustrate the mode-mix. For each structure with different loading conditions, the following equation forms are used to conduct linear regression analysis.

$$\left(\frac{\sigma_{0n}}{\sigma_{0cn}}\right)^{\alpha} + \left(\frac{\sigma_{0t}}{\sigma_{0ct}}\right)^{\beta} = 1$$
 [1]

$$\left(\frac{G_{0n}}{G_{0cn}}\right)^{\alpha} + \left(\frac{G_{0t}}{G_{0ct}}\right)^{\beta} = 1$$
 [2]

In these equations, the σ_{0n} (G_{0n}) and σ_{0t} (G_{0t}) are the peak normal and tangential stresses (toughness) while the σ_{0cn} , σ_{0ct} (G_{0cn} , G_{0ct}) are critical values shown in Figure 21. α and β are the constants controlling the shape of the elliptical curves.

From the mode-mix for stresses shown in Figure 21(a, c), curves for Comb structures show similar shapes but smaller critical values compared with Tight structures, this means a similar level of mode-mix. As for the Loose structures, the structures with zigzag material orientations have

similar mode-mix with other structures while the armchair structure has a much larger value along the normal direction than the tangential.

For the toughness shown in Figure 21(b, d), strong material orientation effects are observed. For the structures with armchair material orientations, the Comb and Loose structures have the same level of critical normal and tangential critical values that are much lower than that of Tight structures, indicating the superior properties against fracture for Tight Ti₃C₂-TiO₂ structures along armchair directions. As for the zigzag structures, the shape of the toughness curve for Comb structures is similar to the Loose structure but with larger critical values. Meanwhile, the Tight structure has the largest normal toughness but the lowest tangential toughness, when compared to the other two structures.

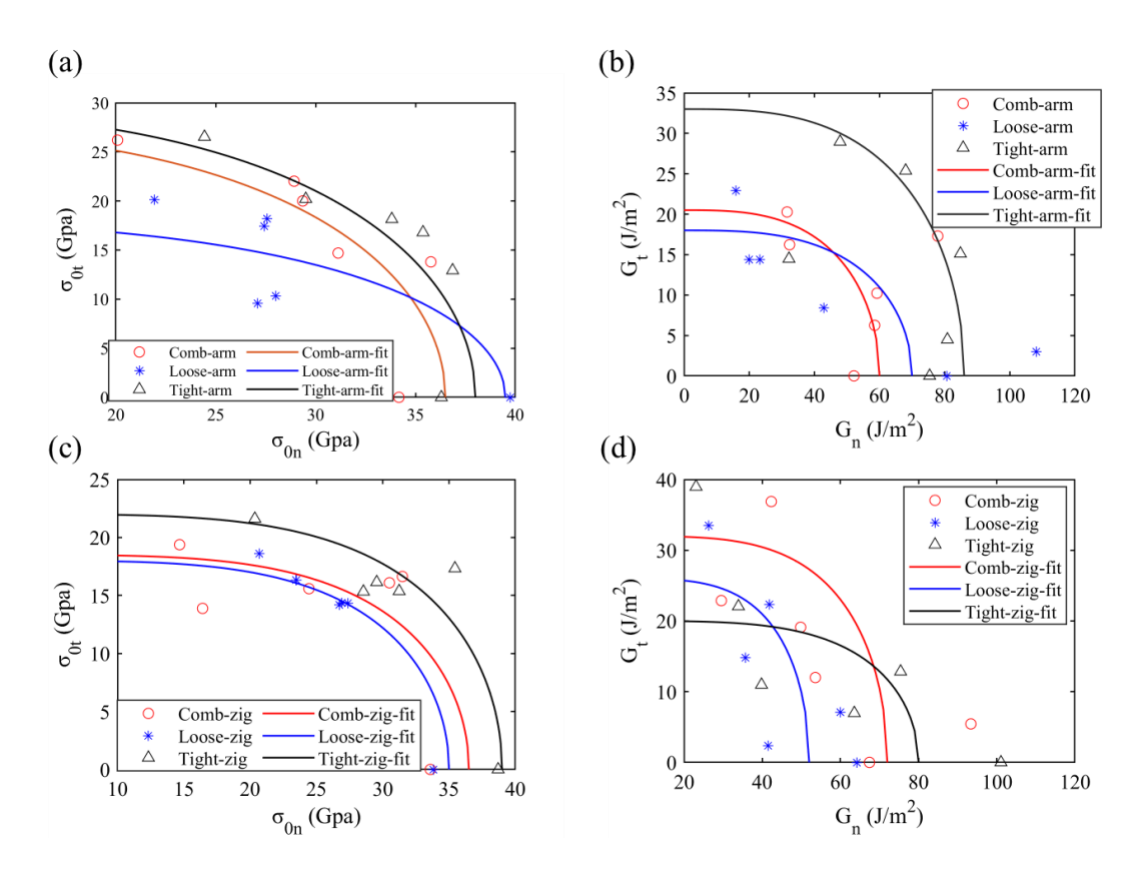


Figure 21. Development of mode-mix in terms of (a and c) normal σ_{0n} and shear stress σ_{0t} , (b and d) and fracture energy.

5. Conclusions and future work

Like other 2D materials, Ti₃C₂ with TiO₂ layers attached above and below exhibits directional properties and fracture behavior. Due to the varying angles of bonds as well as the distances at the interface between TiO₂ layers and Ti₃C₂, the three structures (Comb, Loose, Tight) display distinct characteristics. Through numerical modeling of the deformation and fracture behaviors on nanoribbon and pre-cracked single-layer structures, and following conclusions are obtained:

Anisotropic behavior. Material orientation effects on the fracture behavior are more significant for structures along the armchair direction, where the cohesive zone and Γ_s for the Loose structure are greater than those for the Tight structure. However, in the zigzag direction, both values for Tight are relatively larger.

Asymmetry effects. The asymmetry in the Comb structure, resulting from the different TiO₂ layers on each side, causes asymmetrical effects. During the stretching process, this asymmetry leads to further distortion of the material, resulting in a larger cohesive zone size compared to the previous two structures. Additionally, as the crack propagates, an increasing trend is observed.

Interface connection. The TiO₂ layers in all three structures are connected to MXene through Ti-O bonds. In Figure 1(d-f), the orientation of Ti-O bonds at the interface is perpendicular to the armchair direction in the Loose structure, while in the Tight structure, the angle is acute. The interface bond angles contribute to the ability of the Tight structure to withstand greater loading. Our future work will be devoted to studying other factors that may influence the deformation and fracture properties of Ti₃C2-TiO₂ composites, including other possible crystalline structures based on experimental results, vacancies, defects, oxidation as well as multilayer effects.

Future study. With the new insights, the future study will focus on the oxidation evaluation of existing MXene-TiO₂ thin films under varying oxidation environments. Particular interests in the change of electro-chemical properties will also be explored.

Reference

- 1. Naguib, M., et al., Two-dimensional transition metal carbides. 2012. **6**(2): p. 1322-1331.
- 2. Shahzad, F., et al., *Electromagnetic interference shielding with 2D transition metal carbides (MXenes)*. 2016. **353**(6304): p. 1137-1140.
- 3. Han, M., et al., *Ti3C2 MXenes with modified surface for high-performance electromagnetic absorption and shielding in the X-band.* 2016. **8**(32): p. 21011-21019.
- 4. Mashtalir, O., et al., *Intercalation and delamination of layered carbides and carbonitrides.* 2013. **4**(1): p. 1716.
- 5. Er, D., et al., *Ti3C2 MXene as a high capacity electrode material for metal (Li, Na, K, Ca) ion batteries.* 2014. **6**(14): p. 11173-11179.
- 6. Firouzjaei, M.D., et al., *MXenes: The two-dimensional influencers*. 2022, Elsevier. p. 100202.
- 7. Fu, W., et al., *Materials and technologies for multifunctional, flexible or integrated supercapacitors and batteries.* 2021. **48**: p. 176-197.
- 8. Yang, Q., et al., Recent Progress of MX ene -Based Nanomaterials in Flexible Energy Storage and Electronic Devices. 2018. **1**(4): p. 183-195.
- 9. Ibrahim, Y., et al., The recent advances in the mechanical properties of self-standing two-dimensional MXene-based nanostructures: Deep insights into the supercapacitor. 2020. **10**(10): p. 1916.
- 10. Lipatov, A., et al., *Elastic properties of 2D Ti3C2T x MXene monolayers and bilayers.* 2018. **4**(6): p. eaat0491.
- 11. Wei, C. and C.J.E.F.M. Wu, *Nonlinear fracture of two-dimensional transition metal carbides (MXenes)*. 2020. **230**: p. 106978.
- 12. Sang, X., et al., Atomic defects in monolayer titanium carbide (Ti3C2T x) MXene. 2016. **10**(10): p. 9193-9200.
- 13. Tang, Y., et al., *MXene nanoarchitectonics: defect engineered 2D MXenes towards enhanced electrochemical water splitting.* 2022. **12**(12): p. 2103867.
- 14. Gouveia, J.D. and J.R.J.P.R.M. Gomes, *Structural and energetic properties of vacancy defects in MXene surfaces*. 2022. **6**(2): p. 024004.
- 15. Yorulmaz, U., et al., *Vibrational and mechanical properties of single layer MXene structures: a first-principles investigation*. 2016. **27**(33): p. 335702.
- 16. Fu, Z., et al., Stabilization and strengthening effects of functional groups in two-dimensional titanium carbide. 2016. **94**(10): p. 104103.
- 17. Zha, X.-H., et al., Role of the surface effect on the structural, electronic and mechanical properties of the carbide MXenes. 2015. **111**(2): p. 26007.
- 18. Panda, S., et al., *MXene based emerging materials for supercapacitor applications: Recent advances, challenges, and future perspectives.* 2022. **462**: p. 214518.
- 19. Urbankowski, P., et al., *Synthesis of two-dimensional titanium nitride Ti 4 N 3 (MXene)*. 2016. **8**(22): p. 11385-11391.
- 20. Zhang, N., et al., Superior structural, elastic and electronic properties of 2D titanium nitride MXenes over carbide MXenes: a comprehensive first principles study. 2018. **5**(4): p. 045004.

- 21. Bark, H., et al., Effective Surface Modification of 2D MXene toward Thermal Energy Conversion and Management. 2023: p. 2300077.
- 22. Ghassemi, H., et al., In situ environmental transmission electron microscopy study of oxidation of two-dimensional Ti 3 C 2 and formation of carbon-supported TiO 2. 2014. **2**(35): p. 14339-14343.
- 23. Zhang, L., et al., *In situ crystallization and growth of TiO 2 nanospheres between MXene layers for improved adsorption and visible light photocatalysis.* 2021. **11**(11): p. 3834-3844.
- 24. Al-antaki, A.H.M., et al., *Vortex fluidic mediated synthesis of TiO2 nanoparticle/MXene composites.* 2020. **6**(4): p. 657-662.
- 25. Wang, H., et al., Facile synthesis of heterojunction of MXenes/TiO2 nanoparticles towards enhanced hexavalent chromium removal. 2020. **561**: p. 46-57.
- 26. Meng, W., et al., Advances and challenges in 2D MXenes: From structures to energy storage and conversions. 2021. **40**: p. 101273.
- 27. Wei, W., et al., *Improvement of the Visible -Light Photocatalytic Performance of TiO2 by Carbon Mesostructures.* 2013. **19**(2): p. 566-577.
- 28. Zhang, W., et al., *Visible-light responsive TiO2-based materials for efficient solar energy utilization*. 2021. **11**(15): p. 2003303.
- 29. Kumar, S.G. and L.G.J.T.J.o.p.c.A. Devi, *Review on modified TiO2 photocatalysis under UV/visible light: selected results and related mechanisms on interfacial charge carrier transfer dynamics.* 2011. **115**(46): p. 13211-13241.
- 30. Zhu, C., et al., Carbon nitride-modified defective TiO2–x@ carbon spheres for photocatalytic H2 evolution and pollutants removal: Synergistic effect and mechanism insight. 2018. **122**(35): p. 20444-20458.
- 31. Yu, J., T. Ma, and S.J.P.C.C.P. Liu, Enhanced photocatalytic activity of mesoporous TiO 2 aggregates by embedding carbon nanotubes as electron-transfer channel. 2011. **13**(8): p. 3491-3501.
- 32. Das, A., et al., *Hierarchical ZnO-TiO2 nanoheterojunction: A strategy driven approach to boost the photocatalytic performance through the synergy of improved surface area and interfacial charge transport.* 2020. **534**: p. 147321.
- 33. Kusiak-Nejman, E. and A.W.J.A.C.B.E. Morawski, *TiO2/graphene-based nanocomposites* for water treatment: A brief overview of charge carrier transfer, antimicrobial and photocatalytic performance. 2019. **253**: p. 179-186.
- 34. Chae, A., et al., *Tunable Ti3C2T x MXene-Derived TiO2 Nanocrystals at Controlled pH and Temperature*. 2022. **38**(41): p. 12657-12665.
- 35. Ma, W., et al., Enhanced dielectric constant and suppressed electrical conductivity in polymer nanocomposite films via loading MXene/TiO2/MoS2 nanosheets. 2022. **48**(8): p. 10447-10457.
- 36. Xu, X., et al., Status and prospects of MXene-based nanoelectronic devices. 2023.
- 37. Riazi, H., et al., *Ti 3 C 2 MXene–polymer nanocomposites and their applications.* 2021. **9**(13): p. 8051-8098.
- 38. Mahmud, S.T., et al., *Multilayer MXene heterostructures and nanohybrids for multifunctional applications: a review.* 2022. **4**(6): p. 1174-1206.

- 39. Xu, L., et al., Interfacial charge transfer and interaction in the MXene/Ti O 2 heterostructures. 2021. **5**(5): p. 054007.
- 40. Ganeshan, K., et al., Structure and dynamics of aqueous electrolytes confined in 2D-TiO2/Ti3C2T2 MXene heterostructures. 2020. **12**(52): p. 58378-58389.
- 41. Debow, S., et al., *Charge dynamics in TiO2/MXene composites*. 2021. **125**(19): p. 10473-10482.
- 42. Biswal, L., et al., Review on MXene/TiO2 nanohybrids for photocatalytic hydrogen production and pollutant degradations. 2022. **10**(2): p. 107211.
- 43. Li, Y., et al., Adhesion of two-dimensional titanium carbides (MXenes) and graphene to silicon. 2019. **10**(1): p. 3014.
- 44. Liu, Q., L. Ai, and J.J.J.o.M.C.A. Jiang, *MXene-derived TiO 2@ C/gC 3 N 4 heterojunctions* for highly efficient nitrogen photofixation. 2018. **6**(9): p. 4102-4110.
- 45. Choi, J., et al., *In situ formation of multiple Schottky barriers in a Ti3C2 MXene film and its application in highly sensitive gas sensors.* 2020. **30**(40): p. 2003998.
- 46. Goel, N., A. Kushwaha, and M.J.R.a. Kumar, *Two-dimensional MXenes: recent emerging applications*. 2022. **12**(39): p. 25172-25193.
- 47. Plimpton, S.J.J.o.c.p., *Fast parallel algorithms for short-range molecular dynamics.* 1995. **117**(1): p. 1-19.
- 48. Van Duin, A.C., et al., *ReaxFF: a reactive force field for hydrocarbons.* 2001. **105**(41): p. 9396-9409.
- 49. Kresse, G. and J.J.P.r.B. Furthmüller, *Efficient iterative schemes for ab initio total-energy calculations using a plane-wave basis set.* 1996. **54**(16): p. 11169.
- 50. Perdew, J.P., K. Burke, and M.J.P.r.l. Ernzerhof, *Generalized gradient approximation made simple*. 1996. **77**(18): p. 3865.
- 51. Chenoweth, K., et al., Development and application of a ReaxFF reactive force field for oxidative dehydrogenation on vanadium oxide catalysts. 2008. **112**(37): p. 14645-14654.

Fracture of Ti₃C₂-TiO₂ Atomically Thin Films

Supplementary Information

Jianyu Dai¹, Congjie Wei¹, Chenglin Wu^{1*}

¹ Zachry Department of Civil and Environmental Engineering, Texas A&M University, College Station, TX, USA

Table S1. The flatness differences between the O atoms in outmost atomic layers

Туре	Flatness differences (Angstrom)			
	Loose	Tight	Comb	
Top O layer	0.0229	0.0198	0.0586	
Bottom O layer	0.0672	0.0221	0.0178	

Table S2. Total potential energy for optimized unit cells

	Loose	Tight	Comb	Ti ₃ C ₂
Energy (eV, DFT)	-392.9377	-392.7893	-392.6359	-173.7414
Energy (eV, MD, 1K)	-330.3195	- 339.0621	-334.7876	-137.1923
Error (%)	15.94	13.68	14.73	21.04

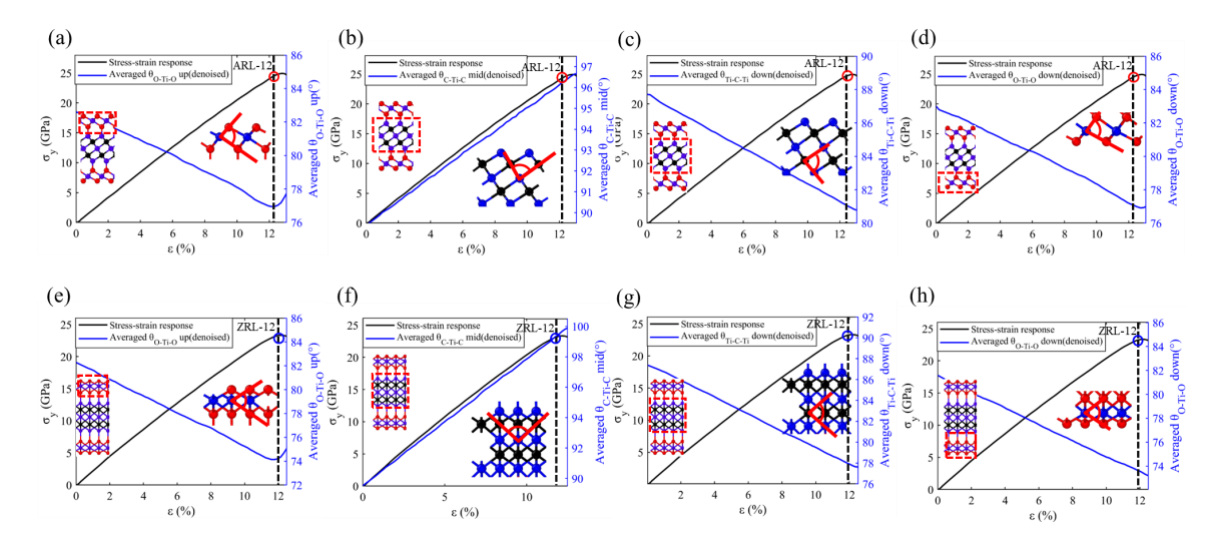


Figure S1. (a–d) $\theta_{O\text{-Ti-O}}$ (top side), $\theta_{C\text{-Ti-C}}$, $\theta_{Ti\text{-}C\text{-Ti}}$, $\theta_{O\text{-Ti-O}}$ (bottom side) regarding strain for Ti₃C₂-TiO₂-Loose nanoribbon stretched along armchair direction. (e-h) $\theta_{O\text{-Ti-O}}$ (top side), $\theta_{C\text{-Ti-C}}$, $\theta_{Ti\text{-}C\text{-Ti}}$, $\theta_{O\text{-Ti-O}}$ (bottom side) regarding strain for Ti₃C₂-TiO₂-Loose nanoribbon stretched along zigzag direction.

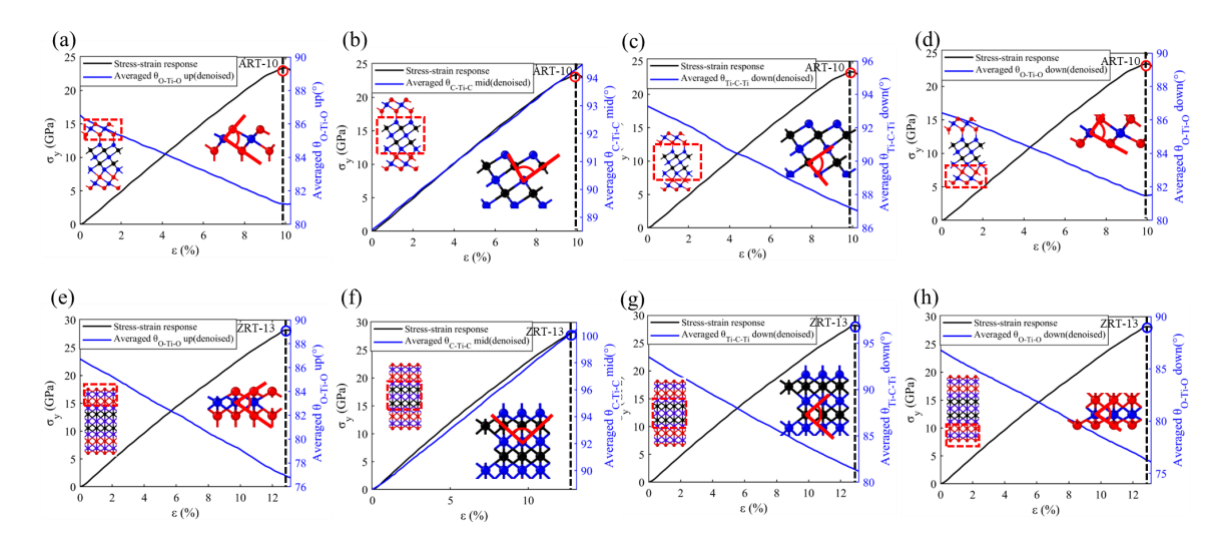


Figure S2. (a–d) $\theta_{O\text{-Ti-O}}$ (top side), $\theta_{C\text{-Ti-C}}$, $\theta_{Ti\text{-C-Ti}}$, $\theta_{O\text{-Ti-O}}$ (bottom side) regarding strain for Ti₃C₂-TiO₂-Tight nanoribbon stretched along armchair direction. (e-h) $\theta_{O\text{-Ti-O}}$ (top side), $\theta_{C\text{-Ti-C}}$, $\theta_{Ti\text{-C-Ti}}$, $\theta_{O\text{-Ti-O}}$ (bottom side) regarding strain for Ti₃C₂-TiO₂-Tight nanoribbon stretched along zigzag direction.

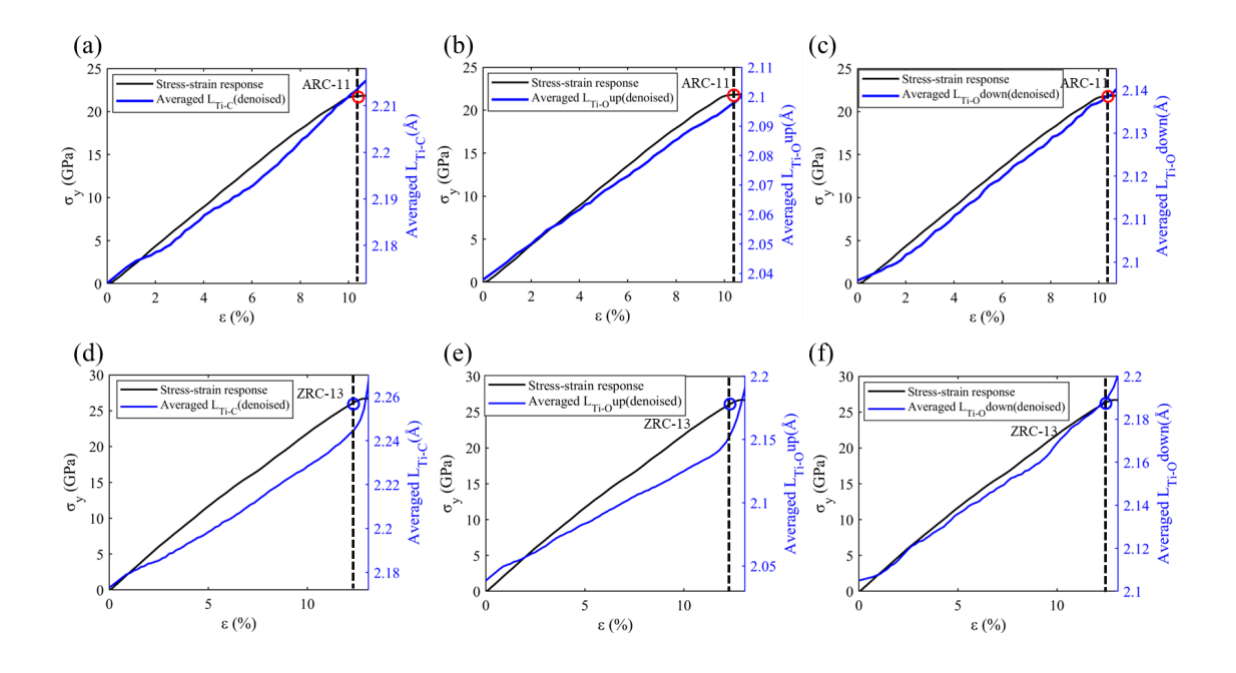


Figure S3. (a–c) L_{Ti-O} (top side), L_{Ti-C} , L_{Ti-O} (bottom side) regarding strain for Ti_3C_2 - TiO_2 -Comb nanoribbon stretched along armchair direction. (d-f) L_{Ti-O} (top side), L_{Ti-C} , L_{Ti-O} (bottom side) regarding strain for Ti_3C_2 - TiO_2 -Comb nanoribbon stretched along zigzag direction.

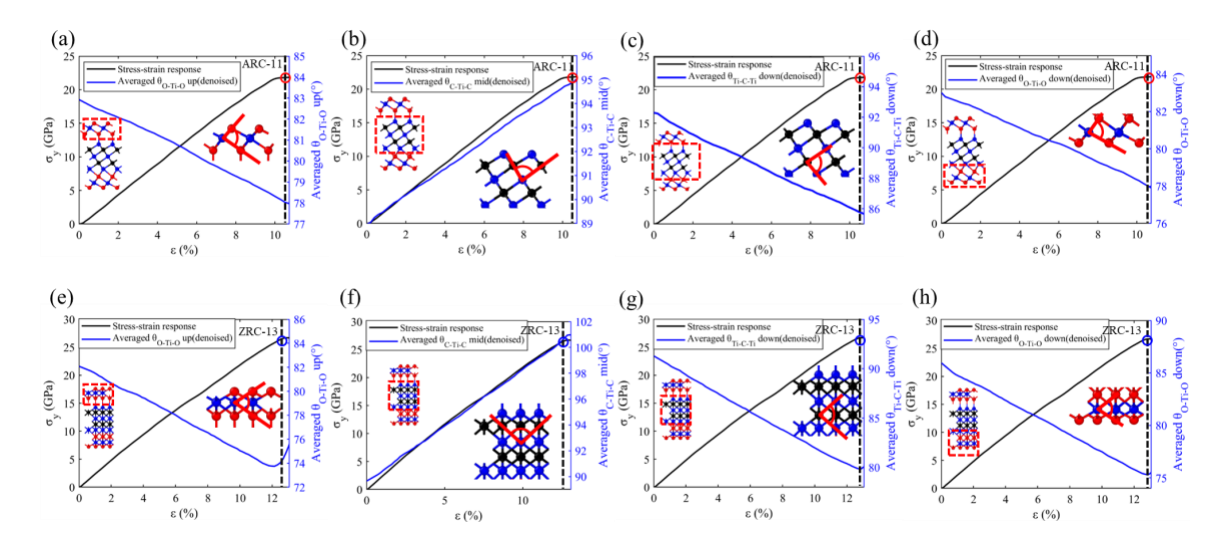


Figure S4. (a–d) $\theta_{O\text{-Ti-O}}$ (top side), $\theta_{C\text{-Ti-C}}$, $\theta_{Ti\text{-}C\text{-Ti}}$, $\theta_{O\text{-Ti-O}}$ (bottom side) regarding strain for Ti₃C₂-TiO₂-Comb nanoribbon stretched along armchair direction. (e-h) $\theta_{O\text{-Ti-O}}$ (top side), $\theta_{C\text{-Ti-C}}$, $\theta_{Ti\text{-}C\text{-Ti}}$, $\theta_{O\text{-Ti-O}}$ (bottom side) regarding strain for Ti₃C₂-TiO₂-Comb nanoribbon stretched along zigzag direction.

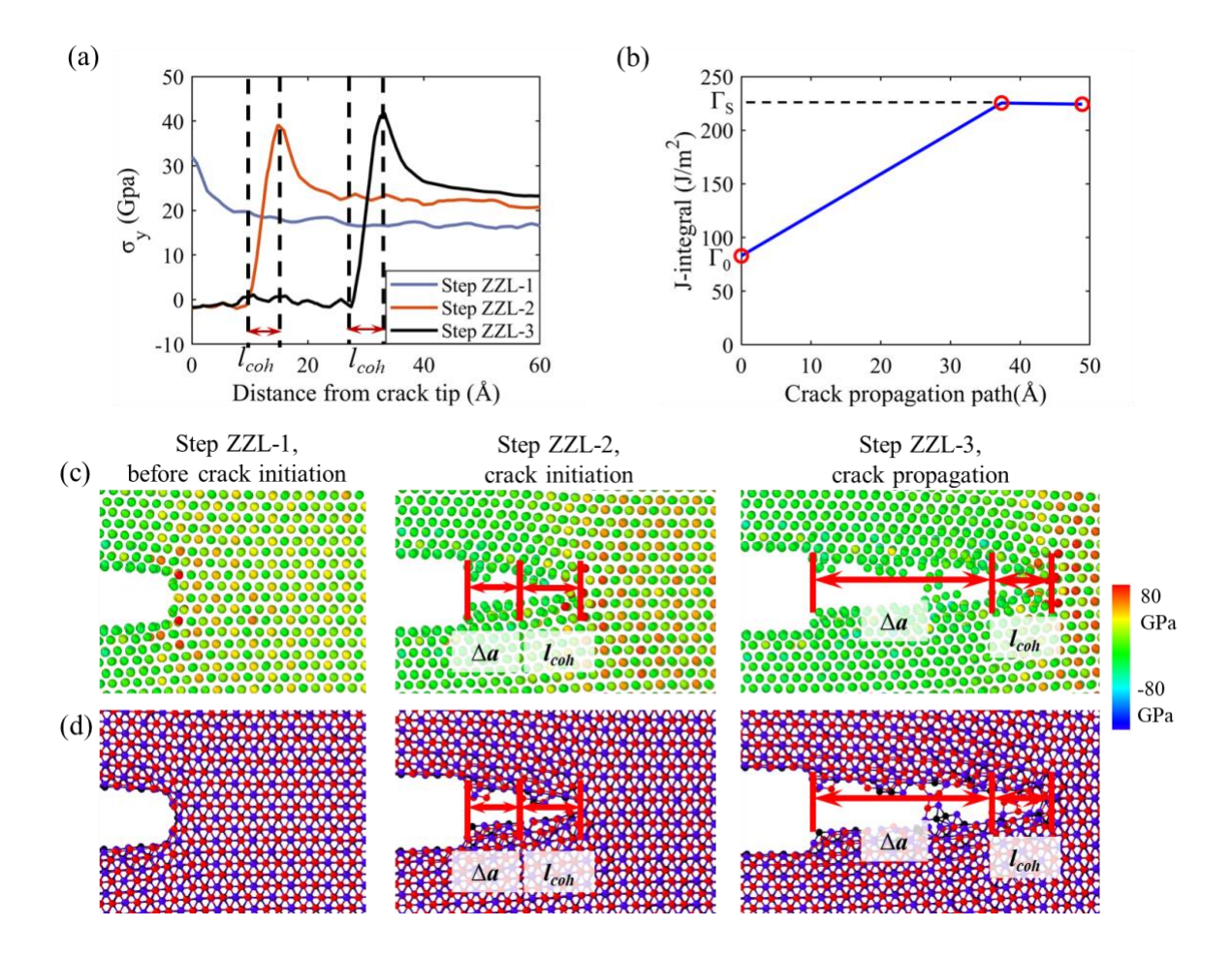


Figure S5. Pre-cracked monolayer Ti_3C_2 - TiO_2 -Loose structure stretched along zigzag direction. (a) σ_{yy} along crack extension direction for different steps. (b) J integral versus crack propagation path. (c) Stress distribution of crack tip area for different steps. (d) Bonding conditions of crack tip area for different steps.

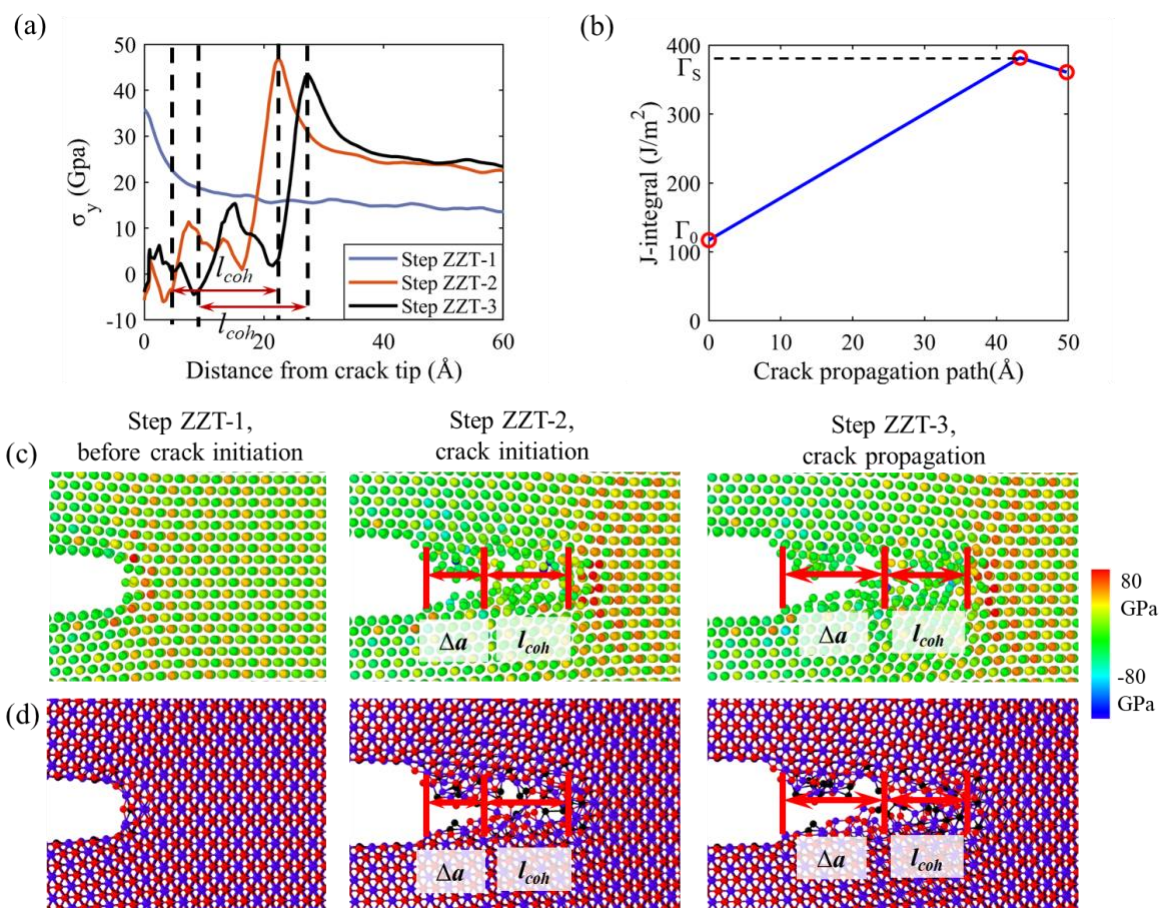


Figure S6. Pre-cracked monolayer Ti_3C_2 - TiO_2 -Tight structure stretched along zigzag direction. (a) σ_{yy} along crack extension direction for different steps. (b) J integral versus crack propagation path. (c) Stress distribution of crack tip area for different steps. (d) Bonding conditions of crack tip area for different steps.

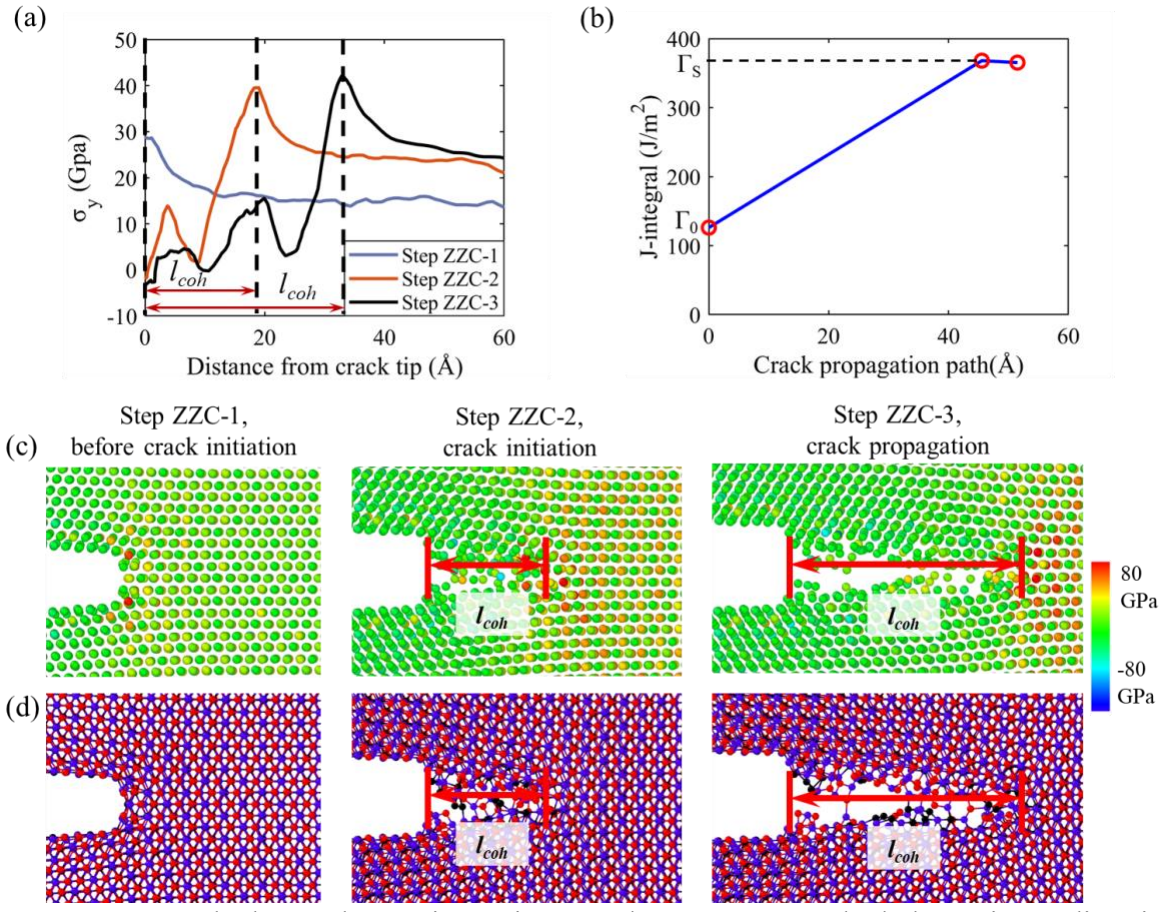


Figure S7. Pre-cracked monolayer Ti_3C_2 - TiO_2 -Comb structure stretched along zigzag direction. (a) σ_{yy} along crack extension direction for different steps. (b) J integral versus crack propagation path. (c) Stress distribution of crack tip area for different steps. (d) Bonding conditions of crack tip area for different steps.

S1. Temperature influence

The influence of temperature change on the mechanical properties of Ti₃C₂ and Ti₃C₂-TiO₂ structures along both material orientations have been explored based on ribbon cases and shown in Figures S8 and S9. Overall speaking, the mechanical properties are degraded by an increasing temperature for all cases. With higher temperature, the Brownian motion of the atoms is promoted, and the bond breaking is more easily to happen. For cases loaded along armchair directions, the influence of temperature on the Young's modulus is limited while the decrease of peak stress is more significant and proportional to the temperature increase. This is verified by the Comb cases with more temperature changes shown in Figure S8b, where the drop at 100k is mostly caused by randomness. Correspondingly, the peak and failure strains also decrease with increasing temperature and show a two-stage behavior with a threshold of 300K. Similar trends are also observed in the cases loaded along zigzag directions. It should be noted that the peak at 300K for the Young's modulus shown in Figure S9b reflects the randomness while the change is limited in a range of 15 GPa, which is only around 6% of the absolute value of Young's modulus.

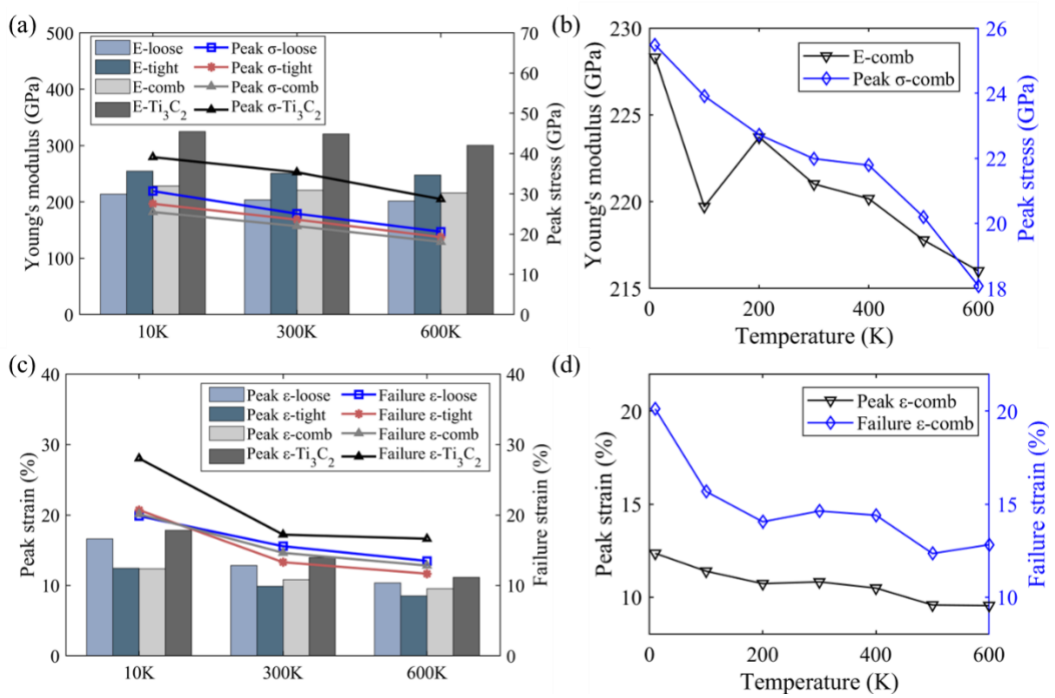


Figure S8. Influence of temperature on the (a) Young's modulus, strength and (c) peak and failure strain of Ti₃C₂ and Ti₃C₂-TiO₂ thin films along armchair direction. Enriched results with more temperature variations for the Comb structure.

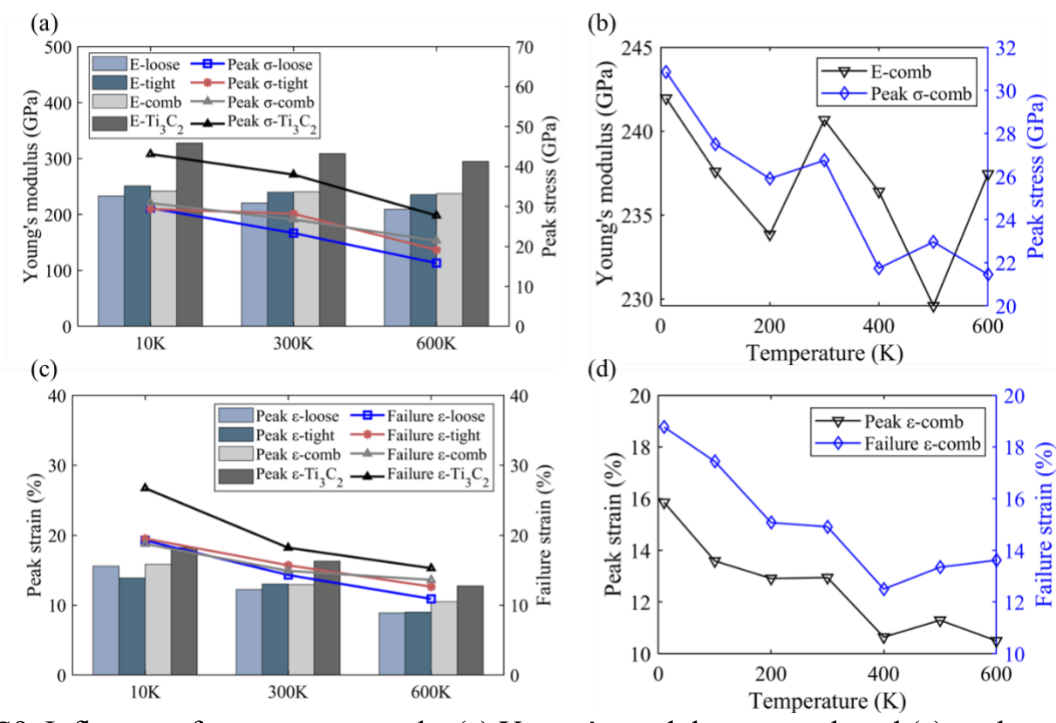


Figure S9. Influence of temperature on the (a) Young's modulus, strength and (c) peak and failure strain of Ti_3C_2 and Ti_3C_2 - TiO_2 thin films along zigzag direction. Enriched results with more temperature variations for the Comb structure.